Scalar spectral functions from the spectral functional renormalization group

Jan Horak,[1] Friederike Ihssen,[1] Jan M. Pawlowski,[1,2] Jonas Wessely,[1] and Nicolas Wink[3]
[1]*Institut für Theoretische Physik, Universität Heidelberg, Philosophenweg 16, 69120 Heidelberg, Germany*
[2]*ExtreMe Matter Institute EMMI, GSI, Planckstraße 1, D-64291 Darmstadt, Germany*
[3]*Institut für Kernphysik (Theoriezentrum), Technische Universität Darmstadt, D-64289 Darmstadt, Germany*

(Received 28 July 2023; accepted 26 July 2024; published 5 September 2024)

We compute spectral functions in a scalar ϕ^4-theory in three spacetime dimensions via the spectral functional renormalization group. This approach allows for the direct, manifestly Lorentz covariant computation of correlation functions in Minkowski spacetime, including a physical on-shell renormalization. We present numerical results for the spectral functions of the two- and four-point correlation functions for different values of the coupling parameter. These results agree very well with those obtained from another functional real-time approach, the spectral Dyson-Schwinger equation.

DOI: 10.1103/PhysRevD.110.056009

I. INTRODUCTION

We set up the spectral functional renormalization group (fRG) for a scalar ϕ^4-theory in three spacetime dimensions. The spectral fRG is a functional real-time approach for the direct computation of correlation functions in Minkowski spacetime. It is based on the general functional real-time setup introduced in [1–4], first applied to Dyson-Schwinger equations (DSEs). For a recent bound-state analysis with the spectral Bethe-Salpeter equation, see [5]. The approach is based on the Källén-Lehmann spectral representation [6,7] for the two-point function, which allows us to analytically access the momentum structure of functional diagrammatic expressions. The setup has been extended to the fRG approach by using a masslike Callan-Symanzik (CS) regulator in [8] and has been applied to gravity in [9]. The CS regulator sustains spectral representations along with Lorentz invariance, and it allows for a spectral renormalization consistent with all symmetries at hand; for more details, see [1,8], and for other applications of the functional Callan-Symanzik equation, see [10–12]. Moreover, in [8], the concept of flowing renormalization has been introduced, which allows for an on-shell renormalization at each renormalization group scale. For further real-time applications of the fRG in a broad variety of research fields, see, e.g., [9,13–31]. Further real-time computations include nondirect reconstruction methods, which utilize Euclidean data to estimate the respective real-time correlation functions. For recent results, see, e.g., [32,33].

In the present work, we accompany the conceptual progress made in [8] with an application to spectral functions in the three-dimensional ϕ^4-theory. This allows us to directly compare our results with those obtained in [1] within the spectral DSE approach. Both functional approaches implement different resummation schemes for the correlators of the given theory through infinite towers of one-loop (fRG) or two-loop (DSE) exact diagrammatic relations. Within an fRG implementation, the successive momentum-shell integration of loop momenta $p^2 \approx k^2$ with the infrared cutoff scale k already provides an average momentum dependence within simple approximations. Due to their intricate spectral representation, this is particularly beneficial for including nontrivial vertices into the flow, e.g., via momentum-independent but cutoff-dependent approximations.

This work is organized as follows: In Sec. II, we briefly discuss the spectral functional approach. In Sec. III, we set up its application to the functional renormalization group for a scalar theory. After discussing the different phases of the theory in Sec. IV, we present our results in Sec. V. This includes a detailed comparison to those obtained with the spectral DSE in [1]. We summarize our findings in Sec. VI.

II. SPECTRAL FUNCTIONS AND FUNCTIONAL EQUATIONS

The central idea of spectral functional approaches is to use the spectral representation for all propagators and vertices in the nonperturbative loop diagrams. Then, the momentum integrals can be performed analytically, and the

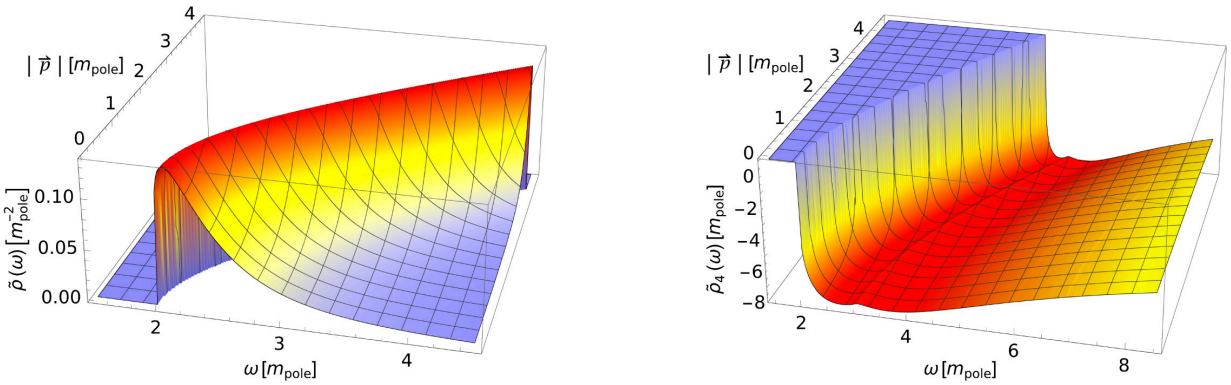

FIG. 1. Propagator and vertex scattering spectra in a $(1+2)$-dimensional ϕ^4-theory in the broken phase. All quantities are measured in units of the pole mass, with a coupling strength $\lambda/m_{\mathrm{pole}} = 20$. (a) Scattering tail of the propagator spectral function as a function of frequency and spatial momentum in the $(1+2)$-dimensional ϕ^4-theory in the broken phase. It features a sharp onset at the $1 \to 2$ particle onset and explicit Lorentz invariance. Higher scattering onsets are strongly suppressed. (b) Spectrum of the resummed four-vertex in an s-channel approximation as a function of frequency and spatial momentum. It features Lorentz invariance and exhibits a sharp onset at the two-particle threshold. The scattering spectrum also has a visible three-particle onset at $3m_{\mathrm{pole}}$.

remaining numerical task boils down to the solution of real spectral integrals.

Most of the relations in the present section can be generalized straightforwardly to general field theories. For the sake of simplicity, we already restrict ourselves to a ϕ^4-theory in $(1+2)$ dimensions, for which also the explicit numerical results in the present work are obtained. Its classical action reads

$$S[\phi] = \int \mathrm{d}^3x \left\{ \frac{1}{2}\phi(-\partial^2 + \mu)\phi + \frac{\lambda_\phi}{4!}\phi^4 \right\}. \tag{1}$$

For $\mu > 0$, the minimum of the classical potential is at vanishing field. Then, the mass parameter can be identified with the classical mass squared, $m_\phi^2 = \mu$. For $\mu < 0$, the full potential exhibits nontrivial minima, and the classical mass of the theory follows from the effective potential as $m_\phi^2 = -2\mu$.

A. Spectral properties of the two-point function

The spectral representation of the propagator of a given field ϕ is at the core of the spectral functional approach. In the present work, we assume the Källén-Lehmann (KL) representation of the full propagator $G(p_0, \vec{p})$ of the field ϕ to hold:

$$G(p_0, \vec{p}) = \int_{0_-}^{\infty} \frac{\mathrm{d}\lambda}{\pi} \frac{\lambda \rho(\lambda, \vec{p})}{\lambda^2 + p_0^2}, \tag{2a}$$

where 0_- ensures that massless poles are taken into account properly. The spectral function $\rho(\lambda)$ is the probability density of creating a Fock state with energy λ from the vacuum in the presence of the quantum field ϕ. It is related to the propagator by

$$\rho(\omega, \vec{p}) = 2\mathrm{Im}G(p_0 = -\mathrm{i}(\omega + \mathrm{i}0^+), \vec{p}). \tag{2b}$$

The propagator is a function of p^2 due to Lorentz symmetry. This allows us to drop any explicit $\vec{p}$ dependence from now on and identify $p_0^2 = p^2$.

The spectral function ρ encodes all dynamical, perturbative, and nonperturbative information of the propagator.

In Eq. (2), p_0 denotes the Euclidean and ω the Minkowski frequency. In the absence of higher-order resonances, the spectral function of the ϕ^4-theory is given by

$$\rho(\omega) = \frac{2\pi}{Z_\phi}\delta(\omega^2 - m_{\mathrm{pole}}^2) + \theta(\omega^2 - m_{\mathrm{scat}}^2)\tilde{\rho}(\omega), \tag{3}$$

with $\rho(\omega) = \rho(\omega, 0)$ and $\tilde{\rho}(\omega) = \tilde{\rho}(\omega, 0)$ for the scattering continuum $\tilde{\rho}$. The mass m_{pole} in Eq. (3) is the pole mass of the full quantum theory, defined by $G^{-1}(\pm m_{\mathrm{pole}}, 0) = 0$.

The scattering continuum sets in at $\lambda^2 = m_{\mathrm{scat}}^2$. In the case of a nonvanishing background field, the theory admits $1 \to 2$ scattering (broken phase), and we have $m_{\mathrm{scat}} = 2m_{\mathrm{pole}}$. Figure 1(a) shows the full scattering tail of the propagator as a function of the frequency ω and spatial momentum $|\vec{p}|$ in the broken phase. Higher thresholds of $1 \to N$ scattering processes lead to further discontinuities in the scattering tail and are typically strongly suppressed. In the absence of $1 \to 2$ scatterings (symmetric phase), the first allowed scattering is $1 \to 3$, and the scattering threshold is $m_{\mathrm{scat}} = 3m_{\mathrm{pole}}$; the respective spectral function is depicted in Fig. 9 and discussed there.

If the spectral representation in Eq. (2) holds, all nonanalyticities of the propagator lie on the real frequency axis. These nonanalyticities are given by either poles or cuts. Poles originate from asymptotic states that overlap with the

propagator of the field ϕ, while cuts represent scattering states.

For the propagator of a physical field that describes an asymptotic state, the spectral function is positive. Furthermore, the canonical commutation relations imply a normalization via the sum rule,

$$\int_{0_-}^{\infty} \frac{\mathrm{d}\lambda}{\pi} \lambda \rho(\lambda, \vec{p}) = 1, \tag{4}$$

for all spatial momenta. Inserting the spectral function (3) into (4), we arrive at

$$\frac{1}{Z_\phi} = 1 - \int_{m_{\mathrm{scat}}}^{\infty} \frac{\mathrm{d}\lambda}{\pi} \lambda \tilde{\rho}(\lambda, \vec{p}). \tag{5}$$

Equation (5) comprises the well-known property that the on-shell amplitude $1/Z_\phi$ is bounded from above by unity, $Z_\phi \geq 1$, as the scattering tail carries part of the total probability.

B. Spectral properties of the four-point function

Vertices also admit spectral representations, which get increasingly complicated for higher-order correlation functions due to their increase in arguments. In the present case, we restrict ourselves to an s-channel approximation of the full one-particle irreducible (1PI) four-point function or vertex. This leaves us with a single momentum argument and an accordingly simple spectral representation. The four-point function is given by the fourth field derivative of the effective action $\Gamma[\phi]$, whose nth field derivatives $\Gamma^{(n)}[\phi]$ are the 1PI n-point functions. We use a spectral representation for this s-channel vertex [1],

$$\begin{aligned} \Gamma^{(4)}(p_0, \vec{p}) &= \lambda_\phi + \int_\lambda \frac{\rho_4(\lambda, \vec{p})}{\lambda^2 + p_0^2}, \\ \rho_4(\omega, \vec{p}) &= 2\mathrm{Im}\Gamma^{(4)}(p_0 = -\mathrm{i}(\omega + \mathrm{i}0^+), \vec{p}), \end{aligned} \tag{6}$$

where λ_ϕ is the classical vertex in Eq. (1) and

$$\int_\lambda = \int_{0_-}^{\infty} \frac{\mathrm{d}\lambda}{\pi} \lambda. \tag{7}$$

Analogously to the spectral function of the propagator, ρ_4 is defined by the discontinuities of the four-point function; see Eq. (6). Also, for the four-point function, the spatial momentum dependence of the spectral function $\rho_4(\omega, \vec{p})$ follows from the function at vanishing spatial momentum, $\rho_4(\omega) = \rho_4(\omega, 0)$ via a Lorentz boost.

Figure 1(b) shows the spectrum of the four-point function in the s-channel approximation discussed in Sec. IV. It shows the $2 \to 2$ scattering onset at twice the pole mass m_{pole} of the field ϕ. The next threshold from the $2 \to 3$ scattering is also visible, but the result also contains the strongly suppressed threshold of higher-order scattering processes. A more detailed discussion of our results is given in Sec. V.

C. Structural properties of diagrams

In the spectral functional approach, spectral representations are utilized to rewrite diagrams in terms of momentum loop integrals over classical propagators with spectral masses and residual spectral integrals; for a general discussion, see [1]. In the present work, we apply this approach in the context of the functional renormalization group, amounting to the *spectral fRG* approach detailed in Sec. III. This leads to one-loop exact relations for correlation functions in terms of full propagators and vertices. In addition, we use a one-loop closed, resummed Bethe-Salpeter kernel to compute the four-point function.

As discussed above, the spectral fRG leads to perturbative one-loop momentum integrals in diagrams, which can be solved analytically. The nonperturbative information of the diagrams, such as pole masses and thresholds, is stored in the remaining spectral integrals. For the present purpose, it is sufficient to consider a single external momentum argument, which is either that of the propagator or the s-channel momentum of the four-point function. However, the generalization to diagrams with several external momenta, as present in the spectral computations of general n-point functions, is straightforward.

In the present case, we only have to consider diagrams with one inflowing or outflowing external momentum $\pm p$, and we encounter diagrams of the general form

$$D[p] = g \int_q \mathrm{Vert}(p, q) \prod_{j=1}^{N} G(l_j), \tag{8}$$

where $l_i = q, q \pm p$ are the momenta of the N propagators, and we have used the abbreviation

$$\int_q = \int \frac{\mathrm{d}^d q}{(2\pi)^d}. \tag{9}$$

$\mathrm{Vert}(p, q)$ carries the momentum dependence of all vertices, which we assume to be either a polynomial or rational function of p and the l_i, or to admit a spectral representation. All prefactors are collected in the overall prefactor g. By inserting the spectral representation in Eq. (2) for each propagator, the momentum integrals acquire a standard perturbative form, where the masses are the respective spectral parameters squared, λ_i^2. Finally, the spectral parameters are integrated over, weighted by the respective spectral function,

$$D[p] = g \prod_{j=1}^{N} \int_{\lambda_j} \rho(\lambda_j) I(\lambda_1, \ldots, \lambda_N, p), \tag{10}$$

with

$$I(\lambda_1,\ldots,\lambda_N,p)=\int_q \mathrm{Vert}(p,q)\prod_{j=1}^{N}\frac{1}{\lambda_j^2+l_j^2}. \quad (11)$$

The momentum integral in (11) is readily solved, and the resulting analytic expression holds true for $p\in\mathbb{C}$. This gives us access to the spectral function Eq. (2) via the limit $p\to -\mathrm{i}(\omega+\mathrm{i}0^+)$. We remark that in the present spectral fRG approach to the $(1+2)$-dimensional scalar theory, all integrals are finite, and we can safely change the order of integration even prior to renormalization. In general, the interchange of momentum and spectral integration performed in (10) assumes a suitable regularization of the full integral, which can be done with *spectral renormalization* [1].

The spectral structure of the diagrams allows for a simple discussion of the emergent scattering thresholds that can be easily tracked within spectral functional approaches. An illustrative example is given by the contribution of the vacuum polarization diagram to the spectral function of a single scalar field: It features a branch cut that opens at the sum of the spectral masses of the two propagators. The spectral function entering the diagram consists of a mass pole at m_{pole} and a sum of scattering continua ρ_N starting at Nm_{pole} with $N\geq 2$. It follows straightforwardly from the analytic structure of that diagram that substituting scattering contributions ρ_N and ρ_M for the two internal lines directly yields a contribution to ρ_{N+M}. This demonstrates how any scattering structure, once seeded, gives rise to higher scattering contributions.

III. SPECTRAL FUNCTIONAL RENORMALIZATION GROUP

In the spectral fRG approach put forward in [8,9], the quantum effective action of the theory at hand is obtained by starting with a theory with an asymptotically large classical pole mass $m_\phi\to\infty$, and then lowering the mass successively until the physical point is reached. The respective classical action is given by Eq. (1), with

$$S[\phi]=\int \mathrm{d}^3x\left\{\frac{1}{2}\phi(-\partial^2+Z_\phi\mu)\phi+\frac{\lambda_\phi}{4!}\phi^4\right\}, \quad (12)$$

with positive or negative μ. The wave function Z_ϕ has been introduced for convenience, anticipating the emergence of a wave function. For asymptotically large pole masses, we have $Z_\phi\to 1$; see Fig. 2(b). Then, (12) reduces to (1), and the pole mass is given by

$$m_\phi^2=\mu-3\mu\theta(-\mu), \quad (13)$$

capturing both the symmetric and broken phases. This setup captures both theories deep in the symmetric phase with $\mu\to+\infty$ and theories deep in the broken phase with $\mu\to-\infty$.

A. Functional Callan-Symanzik equation

The infinitesimal change of the quantum effective action $\Gamma[\phi]$ under a change of the mass μ is governed by the manifestly finite, *renormalized* Callan-Symanzik equation [8,9],

$$\mu\partial_\mu\Gamma[\phi]=\frac{1}{2}\left(1-\frac{\eta_\phi}{2}\right)Z_\phi\mu\mathrm{Tr}[G[\phi]+\phi^2]-\frac{1}{2}\mu\partial_\mu S_{\mathrm{ct}}[\phi], \quad (14a)$$

with the anomalous dimension

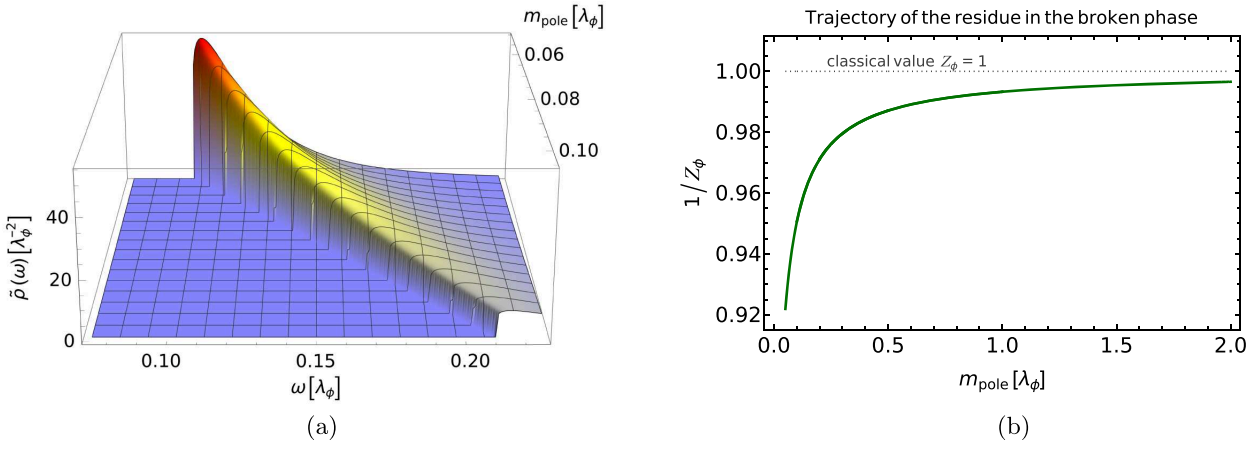

FIG. 2. Spectral function ρ Eq. (21) for different pole masses $m_{\mathrm{pole}}/\lambda_\phi$, measured in the fixed coupling λ_ϕ. (a) Scattering tail $\tilde{\rho}_k$ for vanishing spatial momentum $\vec{p}=0$ as a function of the spectral value ω and the pole mass m_{pole} for $1/20\leq m_{\mathrm{pole}}/\lambda_\phi\leq 1/10$. (b) Amplitude $1/Z_\phi$ of the pole contribution of the spectral function (21) as a function of the pole mass m_{pole} for $1/20\leq m_{\mathrm{pole}}/\lambda_\phi\leq 1/2$. The classical value for Z_ϕ is indicated in gray.

$$\eta_\phi = -2\frac{\mu\partial_\mu Z_\phi}{Z_\phi}, \tag{14b}$$

and the argument ϕ being the mean field which is given by the expectation value of the quantum field φ; i.e., $\phi = \langle\varphi\rangle$. The right-hand side depends on the full field-dependent propagator, which is given in the momentum basis by

$$G[\phi](p,q) = \langle\varphi\varphi\rangle_c(p,q) = \frac{1}{\Gamma^{(2)}[\phi]}(p,q), \tag{14c}$$

where the subscript c refers to the connected part of the two-point function. The first term on the right-hand side of Eq. (14a) is the standard one-loop exact contribution to the flow of the effective action that arises from the variation of the mass in the classical action. It was first derived by Symanzik in [34] in the framework of renormalized perturbation theory, where the UV divergences cancel order by order in the perturbative parameter. In nonperturbative flow equations, this is not sufficient. Starting from nonperturbative finite flow equations with a UV-regulating cutoff, one can analyze a combined RG step of the IR and UV regularization scale, where a change in the latter evidently induces a second term in the flow equation that governs the flow of correlation functions with the UV cutoff. This term can be used to impose explicit renormalization conditions, which are usually set implicitly by the initial condition of the IR flow. Most importantly, as demonstrated in [8], it removes the UV-divergent terms of the diagrams associated with the flow of the mass parameter and renders the CS limit *finite*, where the UV regularization scale is taken to infinity. In the process, it leads to the term $\mu\partial_\mu S_{\rm ct}[\phi]$ in the second line of Eq. (14a). It is constituted by the *finite* parts of the UV-cutoff flow that do not vanish. Such a finite term arises for each UV-relevant direction and implements the corresponding renormalization condition. We will refer to these as counterterm flows. The derivation of (14a) entails its finiteness. Seemingly UV-divergent diagrams only appear as such, due to the compact representation of the CS limit of finite flow equations.

In the momentum basis, the trace in (14a) corresponds to a momentum integral. Note that the effective action $\Gamma[\phi]$ in (14) includes the full mass term $1/2\int_x \mu\phi^2$ in contradistinction to the effective action used in standard fRG momentum-shell flows. There, the momentum-dependent regulator part of the mass term is subtracted, and the physical theory is reached when it vanishes. In the present setup, the μ-dependent effective action is that of a physical theory with mass parameter μ, and the flow is one in (physical) theory space. In contrast to usual momentum-shell flows, this physical flow both is manifestly Lorentz invariant and sustains the causality of physical correlation functions throughout the flow, allowing for the use of the Källén-Lehmann spectral representation Eq. (2).

Compared to the Wetterich equation [35], with a momentum-dependent infrared regularization, the novel ingredient in the functional Callan-Symanzik Eq. (14) is the explicit counterterm flow, $\mu\partial_\mu S_{\rm ct}[\phi]$. The counterterm flow has been derived in a manifestly finite limit of standard momentum cutoff flow equations, as discussed in detail in [8]. This derivation entails that the flow of the counterterm originates from a closed one-loop expression, such as the trace in Eq. (14) itself; i.e., $\mu\partial_\mu S_{\rm ct}[\phi] \sim$ diagrams. Accordingly, the counterterm flow contains no tree-level contributions to the respective correlation functions. This entails that classical values of the correlation functions are solely given by the respective choice of tree-level values specified in the classical action Eq. (12), and in particular cannot be further changed by the specification of renormalization conditions. In consequence, the latter can only be used to renormalize the flow contributions, but not the initial conditions of the flow. This excludes, for example, that the counterterm flow rearranges the theory from the symmetric into the broken phase or vice versa by $\mu\partial_\mu S_{\rm ct} \propto \pm\text{const.}\mu\int\phi^2$. However, the counterterm can contain similar terms proportional to $\lambda_\phi/m_{\rm pole} = \lambda_{\rm eff}$.

In particular, the counterterm flow allows for *flowing renormalization conditions*, and we shall use it to adjust a *flowing on-shell renormalization*, based on the spectral on-shell renormalization put forward in [1]. Then, the pole mass $m_{\rm pole}$ is identified with m_ϕ in (13) in both phases: $m^2_{\rm pole} = \mu - 3\mu\theta(-\mu)$. In this physical RG scheme, the phase transition between the symmetric and broken phases happens for $m^2_\phi = 0$. Hence, we approach the phase transition from both the broken and the symmetric phase in the limit $\mu \to 0$, and the flows are taking place in the one or the other phase; see Fig. 3. Thereby, our setup avoids flows through the strongly interacting phase transition regime, which are usually present in momentum cutoff flows. This minimizes the systematic error stemming from the strong dynamics in the vicinity of a phase transition, where the flows are highly sensitive to truncation artifacts. However, it is in principle possible to flow through the phase transition, which can be advantageous if it is difficult to identify a proper starting point in one phase at which the theory is particularly simple. An example for this situation can be found in quantum mechanics, where the theory for $\mu \to -\infty$ does not approach the classical limit, but rather the instanton-dominated regime.

In the present work, we consider the flow of the inverse propagator within the spectral representation. The flow is given by

$$\mu\partial_\mu\Gamma^{(2)}(p^2) = \left(1-\frac{\eta_\phi}{2}\right)Z_\phi\mu\left[D_{\rm pol}(p^2) - \frac{1}{2}D_{\rm tad}(p^2)\right] + \left(1-\frac{\eta_\phi}{2}\right)Z_\phi\mu - \frac{1}{2}\mu\partial_\mu S^{(2)}_{\rm ct}, \tag{15}$$

where $D_{\rm tad}$ and $D_{\rm pol}$ refer to the tadpole and polarization diagrams; see Fig. 5. Their general form, in terms of the

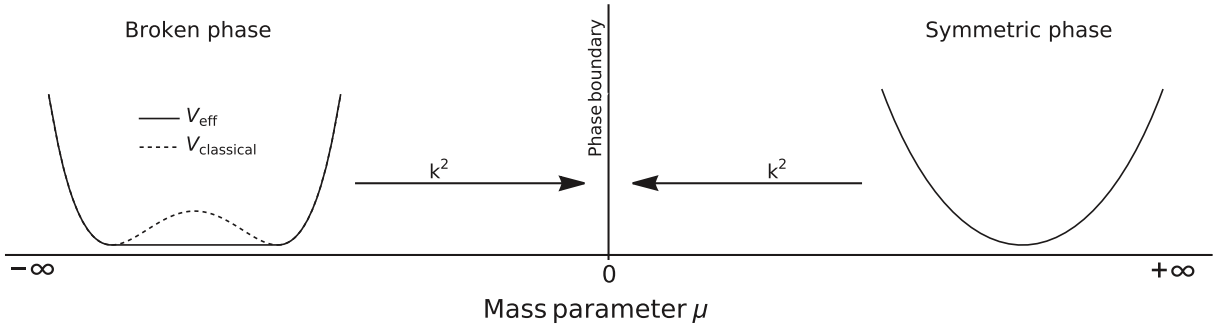

FIG. 3. Schematic phase diagram with respect to the mass parameter μ. The phase boundary is located at $\mu = 0$. The flow is initiated in the deep UV, i.e., $|\mu| = k^2 \to \infty$, with the respective (classical) initial effective potential.

spectral representation for the propagator and four-point function, is discussed in Appendix A. Moreover, all quantities in (15) depend on the chosen background ϕ. For general spacetime-dependent backgrounds $\phi(x)$, this would lead to $\Gamma^{(2)}[\phi](p,q)$. In the explicit computations, we consider the background ϕ_0, which is the constant solution of the equation of motion,

$$\left.\frac{\delta\Gamma[\phi]}{\delta\phi}\right|_{\phi=\phi_0} = 0. \tag{16}$$

With this physical choice for the background, the general field-dependent propagator Eq. (14c) reduces to the physical propagator $G(p^2)$ in the absence of source terms:

$$G(p^2) = \frac{1}{\Gamma^{(2)}[\phi_0](p^2)}. \tag{17}$$

In the symmetric phase, we have $\phi_0 = 0$, while $\phi_0 \neq 0$ signals the broken phase. At constant fields, the propagator

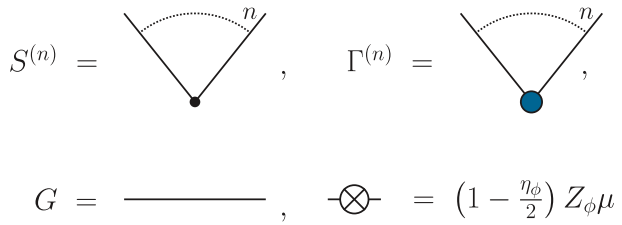

FIG. 4. Diagrammatic notation used throughout this work: Lines stand for full propagators, small black dots stand for classical vertices, and larger blue dots stand for full vertices. The crossed circle represents the scale derivative of the mass parameter.

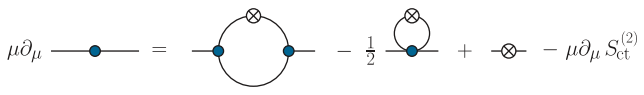

FIG. 5. Renormalized CS equation for the inverse propagator. The notation is given in Fig. 4.

(14c) reduces to $G(p,q) = G(p^2)(2\pi)^d\delta(p+q)$. Similarly, we have $\Gamma^{(2)}[\phi_0](p,q) = \Gamma^{(2)}[\phi_0](p^2)(2\pi)^d\delta(p+q)$.

In three dimensions, the two phases are separated by a second-order phase transition in the Ising universality class. From now on, we drop the field argument ϕ_0. It is implicitly understood that all correlation functions are evaluated at $\phi = \phi_0$.

In a final step, we substitute μ with $\pm k^2$, to keep the relations to standard fRG flows with momentum cutoffs simple, where k is commonly used. This facilitates the comparison and benchmarking of the real-time results obtained with the spectral fRG. For example, the three-dimensional ϕ^4-theory has been studied abundantly within the Euclidean fRG, including systematic studies of the convergence of approximation schemes; for a recent review, see [36]. These results carry over straightforwardly to the present approach, and the Euclidean correlation functions obtained from the spectral functions can be directly compared. This substitution leads us to

$$k^2 = |\mu|, \qquad \partial_t = k\partial_k = 2\mu\partial_\mu, \tag{18}$$

where the (negative) RG time $t = \log(k/k_{\text{ref}})$ is measured relatively to a suitable reference scale or mass.

B. Spectral on-shell renormalization

We proceed with discussing the on-shell spectral renormalization, using the direct access to Minkowskian momenta. In $(1+2)$ dimensions, both diagrams in the CS flow of the inverse propagator (15) are manifestly finite and do not need regularization. The flow of the counterterm action $\mu\partial_\mu S_{\text{ct}}$ only guarantees the implementation of the chosen renormalization conditions. The $(1+2)$-dimensional ϕ^4-theory is super-renormalizable, and it has only one UV-relevant direction. This leaves us with one renormalization condition for the mass. Now, we use on-shell renormalization to keep the full pole mass on the classical input mass (13) with $m^2_{\text{pole}} = k^2$ in the symmetric phase, and $m^2_{\text{pole}} = 2k^2$ in the broken phase. This leads us to

(i) Symmetric phase:

$$\Gamma^{(2)}[\phi_0]\Big|_{p^2=-k^2} = 0. \tag{19}$$

(ii) Broken phase:

$$\Gamma^{(2)}[\phi_0]\Big|_{p^2=-2k^2} = 0. \tag{20}$$

In the symmetric phase, the first allowed scattering process is the $1 \to 3$ scattering, and the onset of the scattering continuum is located at 3 times the pole mass. In turn, in the broken phase with $1 \to 2$ scattering, the onset of the scattering continuum of the spectral function is located at twice the pole mass. Thus, the spectral function (3) reads

$$\rho(\lambda) = \frac{2\pi}{Z_\phi}\delta(\lambda^2 - m_{\rm pole}^2) + \theta(\lambda^2 - m_{\rm scat}^2)\tilde{\rho}(\lambda), \tag{21}$$

with $m_{\rm scat} = 3m_{\rm pole}$ (symmetric phase) and $m_{\rm scat} = 2m_{\rm pole}$ (broken phase). In Fig. 2, we show the scale evolution of the spectral function ρ in the broken phase: in Fig. 2(a), we depict the scattering tail $\tilde{\rho}$, and in Fig. 2(b), we depict the amplitude of the pole contribution. All quantities are measured relative to the coupling λ_ϕ.

The spectral tail is rising toward smaller pole masses for a fixed classical coupling, and in turn the amplitude $1/Z_\phi$ of the pole contribution is decreasing. In combination, the sum rule (4) holds during the evolution. The growing importance of the scattering processes can be understood from the fact that the dynamics of the theory only depend on the dimensionless ratio λ_ϕ/m_ϕ, with $m_\phi \propto k$. Hence, the effective coupling grows strong for smaller pole masses, and on the other hand, the dynamics of the theory are vanishing for asymptotically large pole masses.

In contrast to the Callan-Symanzik or mass regulator used in the present work, commonly used regulators in Euclidean flows decay for momenta larger than the IR cutoff k. This provides manifestly finite flows without the need of further renormalization. Moreover, for Euclidean momenta, the respective flows of lower-order correlation functions decay faster than for a CS regulator. In Minkowski space, however, the CS or mass regulator has the welcoming property that the one-loop flow of $\rho(\omega)$ contains only classical correlation functions and is maximally local. While this is trivial in the symmetric phase, where the one-loop flow only shifts the pole mass and does not generate a scattering continuum, it is nontrivial in the broken phase. There, the flow of the scattering continuum is given by a single delta function at the onset of the scattering spectrum, which originates from $\partial_t {\rm Im}\Gamma^{(2)} \propto \delta(\omega^2 - 4m_{\rm pole}^2)$. Since the mass pole constitutes the dominant part of the propagator, the flow of the spectral function at spectral values larger than the flowing onset $2m_{\rm pole}$, which is solely induced by the scattering tail, is subleading.

C. Flowing with the minimum

In general, the flow equation (14a) can be evaluated for arbitrary values of the external field ϕ, which requires the inclusion of the full effective potential. However, this goes beyond the scope of this work, and we simply evaluate the flow on the solution ϕ_0 of the equation of motion (16). This is a commonly used truncation, as it gives access to the physical correlation functions.

In the present fRG approach with the spectral CS regulator, the flow takes place in theory space, and the effective action is physical for all values of k. In the broken phase, the minimum of the full effective potential depends on k, and the total mass flow of the two-point function is given by the flow diagrams originating from the CS equation, $\partial_t\Gamma^{(2)}[\phi_0](p)$ and a term proportional to the mass flow of ϕ_0,

$$\frac{d}{dt}\Gamma^{(2)}[\phi_0](p) = \partial_t\Gamma^{(2)}[\phi_0](p) + (\partial_t\phi_0\Gamma^{(3)}[\phi_0])(p). \tag{22}$$

The novel ingredient in the present setup originates in the tree-level k dependence of $\phi_0 \approx \sqrt{6k^2/\lambda_\phi} + \mathcal{O}(\lambda_\phi k)$, where the second term comprises the loop corrections. This tree-level dependence is usually absent in the flow of the minimum in standard momentum-shell flows. There, $\partial_t\phi_0$ only comprises the effects of the momentum shell integration, and hence is inherently one-loop and beyond. The tree-level k dependence of ϕ_0 in the present case triggers a tree-level k dependence of $\partial_t\phi_0\Gamma^{(3)}(p)$, and the tree-level flow of the physical two-point function considered here reads

$$\frac{d}{dt}\Gamma^{(2)}\Big|_{\rm tree\text{-}level} = -2k^2 + \partial_t\phi_0 S^{(3)}[\phi_0] = 4k^2, \tag{23}$$

where the classical three-point function is given by $S^{(3)}[\phi] = \lambda_\phi\phi$. Note that only the combination of both terms leads to the expected positive flow of the physical mass, while the flow of the mass parameter $-k^2$ has a negative sign.

To obtain the full momentum structure of the second term in Eq. (22), we first note that the additional leg of the three-point function is always augmented with an incoming momentum of zero, as it is contracted with the scale derivative of a constant field. The full momentum dependence can then be incorporated via the DSE of the three-point function, which allows for an exact diagrammatic flow of the two-point function on the physical minimum. In the presence of approximations, a fully self-consistent treatment would require us to use the integrated flow of $\Gamma^{(3)}[\phi_0](p,0)$. However, the flow of $\Gamma^{(3)}[\phi_0]$ also includes a

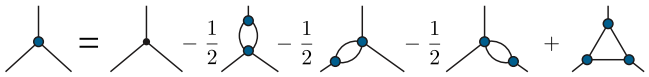

FIG. 6. Truncated DSE for the three-point function in the skeleton expansion. The notation is given in Fig. 4.

similar additional term to (23), which is proportional to the four-point function. To avoid solving the flow of the three- and four-point functions, we resort to the DSE to include the leading momentum dependence of the (contracted) three-point function. To ensure the correct RG scaling of the flow equation, we further employ the skeleton expansion in the DSE, where every vertex is dressed. Approximating $\Gamma^{(n>4)} \approx 0$ and dropping the remaining two-loop diagrams, we arrive at the simple diagrammatic structure of the three-point function depicted in Fig. 6.

Additionally, using the DSE for $\Gamma^{(3)}$ in Eq. (22) demonstrates the structure of the flow as a total derivative. To make this explicit, we choose the vertical leg in Fig. 6 to be contracted with $\partial_t \phi_0$. Then, the three-point functions connected to this leg carry only internal momenta, and we approximate them as constant. With that, the first fish diagram and the triangle diagram in Fig. 6 are proportional to the tadpole and polarization diagrams, respectively, and the second term on the rhs of the flow (22) reads

$$(\partial_t \phi_0 \Gamma^{(3)}[\phi_0])(p) = \partial_t \phi_0 \Big(S^{(3)}[\phi_0] - \frac{1}{2}\Gamma^{(3)}[\phi_0] D_{\text{tad}}(p) - D_{\text{fish}}(p) + \Gamma^{(3)}[\phi_0] D_{\text{pol}}(p) \Big). \quad (24)$$

Note that the explicit three-point functions on the right-hand side are now momentum-independent. For the full expressions of the spectral diagrams, we refer to Appendix A. We discuss our approximations for the remaining vertices in Sec. IV.

Substituting (15) and (24) into (22), we eventually arrive at the full flow equation of the two-point function. Its diagrammatic representation is depicted in Fig. 7. It is illuminating to consider the one-loop structure of the flow, where the nature of the flow being a total derivative can be read from Fig. 7. There, the red crossed circle comprises the total derivative of the internal propagators in the (one-loop) polarization and tadpole diagram, while the fish diagram accounts for the running of the three-point vertices. The full equation reads

$$\frac{d}{dt}\Gamma^{(2)}[\phi_0](p) = (\partial_t \phi_0) S^{(3)}[\phi_0] - (2 - \eta_\phi) Z_\phi k^2 + \dot{\mathcal{R}} \Big[-\frac{1}{2} D_{\text{tad}} + D_{\text{pol}} \Big] - \partial_t \phi_0 D_{\text{fish}} - \partial_t S_{\text{ct}}[\phi_0], \quad (25a)$$

where

$$\dot{\mathcal{R}} = (\partial_t \phi_0 \Gamma^{(3)}[\phi_0] - (2 - \eta_\phi) Z_\phi k^2) \quad (25b)$$

is represented as a red crossed circle in Fig. 7. Note the appearance of a relative minus sign in front of the mass derivative contribution (second term) to Eq. (25b) due to $\mu = -k^2$ in the broken phase. The first line in (25a) carries the trivial, tree-level running of the inverse propagator. It consists of the running of the mass parameter and the classical part of the three-point function, connected to the flow of the minimum. Its mean-field value cannot be altered by the renormalization condition and is, analogously to the respective term in $\dot{\mathcal{R}}$, crucial to recover the correct sign of the flow; see Eq. (23). A detailed evaluation of Eq. (25a) can be found in Appendix B.

IV. APPROXIMATIONS AND REAL-TIME FLOWS IN THE SYMMETRIC AND BROKEN PHASES

In the following section, we discuss the approximations used for the higher correlation functions, which lead to nontrivial spectral flow equations in both phases. This enables us to write down the renormalized flow equations for the two-point function and evaluate them on the real frequency axes.

In the ϕ^4-theory, correlation functions of an odd number of fields, $\Gamma^{(2n+1)}[\phi]$, are proportional to the mean field ϕ. In the present approximation, we only consider three- and four-point functions, setting all the higher correlation functions to zero:

$$\Gamma^{(n>4)} \approx 0. \quad (26)$$

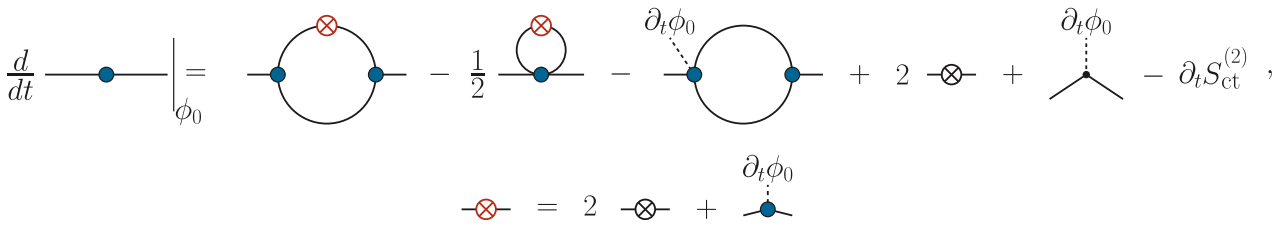

FIG. 7. Diagrammatic representation of the flow of the two-point function on the flowing minimum in the broken phase. The notation is given in Fig. 4. The red crossed circle comprises the scale derivative of the mass parameter and the three-point function, where the additional factor of 2 comes from the change from μ to k. The dashed lines indicate the contraction with $\partial_t \phi_0$.

Then, the three-point function is proportional to a product of the four-point function and ϕ_0. This closes our approximation.

For constant vertices, the tadpole diagram only provides a constant contribution to the flow of the two-point function. This contribution is absorbed completely in the on-shell renormalization conditions, (20) and (19), for the broken and symmetric phases, respectively. In the symmetric phase of the theory with $\phi_0 = 0$, the tadpole is the only contribution to the flow of the two-point function. Hence, the scattering tail originates only from the nontrivial momentum dependence of the four-point function. In a first but important step toward the full momentum dependence of $\Gamma^{(4)}(p_1, \ldots, p_4)$, we use an s-channel resummation of the full four-point function (see Fig. 8):

$$\Gamma^{(4)}(p^2) = \frac{\lambda_\phi}{1 + \frac{\lambda_\phi}{2}\int_q G(p+q)G(q)}. \tag{27}$$

In Eq. (27), $p^2 = s = (p_1 + p_2)^2$ is the s-channel momentum, and we choose vanishing t and u channels to perform the resummation: $(p_3 - p_1)^2 = (p_1 - p_4)^2 = 0$. This approximation admits the simple spectral representation (6) of the four-point function; see also [1].

We emphasize that (27) only holds true in the symmetric phase. In contrast, in the broken phase, the flow or BSE for the four-point function contains additional diagrams with two or four three-point vertices. Their combined contributions are readily estimated and are suppressed by a factor $1/8$. Hence, they are dropped in the following computation. Accordingly, we use (27) in both phases.

Note also that the four-point function exhibits a bound-state pole below $2m_{\rm pole}$ close to the phase transition. This is discussed—for example, in [5,37]—in terms of a Bethe-Salpeter equation, and it is indeed seen in lattice and fRG calculations—see [38–40]. The present s-channel resummation for the four-vertex does not include the resonant channel. A full bound-state analysis and the systematic inclusion of other channels will be considered elsewhere.

It remains to specify the three-point function $\Gamma^{(3)}(p_1, p_2, p_3)$ in Eq. (25a). In contrast to the pivotal importance of the momentum dependence of the four-point function, that of the three-point function is averaged out in the vacuum polarization and the fish diagram. For the sake of simplicity, we therefore approximate the full vertex by its value at vanishing momenta, $p_i = 0$ for $i = 1, 2, 3$. There, the three-point function is given by the third derivative of the effective potential on the equations of motion, $V^{(3)}_{\rm eff}(\phi_0)$. The effective potential $V_{\rm eff}(\phi)$ is the quantum analogue of the classical potential and is simply the effective action $\Gamma[\phi]$, evaluated for constant fields ϕ_c:

$$V_{\rm eff}(\phi_c) = \frac{1}{\mathcal{V}}\Gamma[\phi_c], \qquad \mathcal{V} = \int d^3x. \tag{28}$$

Due to the Z_2 symmetry of the ϕ^4-theory under $\phi \to -\phi$, the effective potential is symmetric, $V_{\rm eff}(-\phi) = V_{\rm eff}(\phi)$. Moreover, it admits an expansion about the solution to the equation of motion, $\phi^2 = \phi_0^2$, which is valid for $\phi^2 \geq \phi_0^2$. The latter constraint on the modulus of $(\phi^2 - \phi_0^2)$ originates from the fact that the classical effective potential is the double Legendre transform of the classical potential. In the case of a nonconvex potential, it is simply the convex hull. Schematically, this is depicted in Fig. 3.

The effective potential satisfies its own flow equation, and for the sake of completeness we briefly discuss its derivation and explicit form in Appendix H; more details can be found in [8]. The present computation can be augmented by the full flow of the effective potential, effectively leading to a cutoff dependence of the coupling λ_ϕ in (27) and similar changes. While this provides further quantitative precision to the computation, it goes beyond the scope of the present work and will be presented elsewhere. Here, we shall consider the expansion up to $(\phi^2 - \phi_0^2)^2$, dropping higher-order terms in accordance with (26), and we shall discuss the symmetric and broken phases separately in Secs. IV B and IV A below.

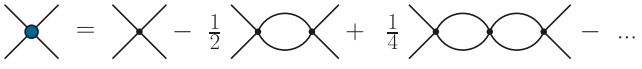

FIG. 8. Bubble resummed four-point function. The notation is given in Fig. 4.

A. Symmetric phase

In the symmetric phase with $\phi_0 = 0$ in Eq. (16), we use a Taylor expansion about $\phi^2 = 0$ for the effective potential,

$$V_{\rm eff}(\phi) = \sum_{n=1}^{\infty} \frac{\lambda_n}{2n!}\phi^{2n}. \tag{29}$$

The first two couplings, λ_1 and λ_2, are related to the correlation functions $\Gamma^{(2)}$ and $\Gamma^{(4)}$ considered here. Hence, the coupling λ_1 agrees with the curvature mass squared in the symmetric phase, where the curvature mass is defined as

$$m^2_{\rm curv} = V^{(2)}_{\rm eff}(\phi_0) = \Gamma^{(2)}[\phi_0](p = 0) \tag{30}$$

in both phases. Moreover, the coupling λ_2 is just the full four-point function, evaluated at vanishing momentum. In summary, we have

$$\lambda_1 = m^2_{\rm curv}, \qquad \lambda_2 = \Gamma^{(4)}(p = 0). \tag{31}$$

For the initial UV pole mass $m_{\rm pole} = \Lambda$, the curvature mass and the pole mass agree, $\lambda_1 = \Lambda^2$, and the initial coupling is the classical one, $\lambda_2 = \lambda_\phi$. Hence, the initial effective potential $V_{\rm UV}(\phi)$ at $k = \Lambda$ reads

$$V_{\mathrm{UV}}(\phi) = \frac{1}{2}\Lambda^2\phi^2 + \frac{1}{4!}\lambda_\phi\phi^4. \tag{32}$$

With the above approximations, all higher correlation functions are fixed, and the flow equation of the two-point function on the real frequency axes reads

$$\partial_t\Gamma^{(2)}(\omega_+) = -\frac{Z_\phi(2-\eta_\phi)k^2}{2} D^{\mathrm{dyn}}_{\mathrm{tad}}(\omega_+) + 2k^2 - \partial_t\hat{S}^{(2)}_{\mathrm{ct}}, \tag{33}$$

where the retarded limit is given by $\omega_+ = -\mathrm{i}(w + \mathrm{i}0^+)$ and is explicitly carried out in Appendix F. $\hat{S}^{(2)}_{\mathrm{ct}}$ is given schematically by

$$\hat{S}^{(2)}_{\mathrm{ct}} = \mathrm{diagrams}(p^2 = -k^2). \tag{34}$$

We denoted the counterterm action with a tilde, since we already dropped constant terms in the flow of order $\lambda_\phi k$. Hence, only the dynamic part of the tadpole $D^{\mathrm{dyn}}_{\mathrm{tad}}$ contributes. It arises from the scattering tail of $\Gamma^{(4)}(p)$ and carries the spectral structure of the polarization diagram; see Eq. (A4). In particular, the deviation of the constant term in Fig. 5 from its classical value, $2k^2$, is of order $(\lambda_\phi k)$ and is therefore absorbed in the renormalization constant. With that, Eq. (33) is consistent with the flowing on-shell renormalization condition (19).

B. Broken phase

In the broken phase with $\phi_0 \neq 0$, we use a Taylor expansion about $\phi^2 = \phi_0^2$ for the effective potential,

$$V_{\mathrm{eff}}(\phi) = \sum_{n=2}^{\infty} \frac{\lambda_n}{2n!}(\phi^2 - \phi_0^2)^n. \tag{35}$$

At vanishing momentum and constant fields, the correlation functions derived from the effective action $\Gamma[\phi_0]$ coincide with the moments of the effective potential. We consider n-point functions for $n \leq 4$ with

$$\begin{aligned}
\Gamma^{(2)}[\phi_0](p=0) &= \frac{1}{3}\lambda_2\phi_0^2, \\
\Gamma^{(3)}[\phi_0](p=0) &= \lambda_2\phi_0 + \frac{\lambda_3}{15}\phi_0^3, \\
\Gamma^{(4)}[\phi_0](p=0) &= \lambda_2 + \frac{2}{5}\lambda_3\phi_0^2 + \frac{1}{105}\lambda_4\phi_0^4,
\end{aligned} \tag{36}$$

In contrast to the symmetric phase discussed in Sec. IV A, higher-order terms with couplings λ_n also contribute due to $\phi_0 \neq 0$. For this reason, we have indicated the ϕ_0 dependence of $\Gamma^{(n)}$ in (36). As discussed below Eq. (17), we generically drop the ϕ_0 dependence for the sake of readability; it is implicitly assumed that all expressions are evaluated at ϕ_0.

As a consequence of Eq. (26), all expansion coefficients λ_n with $n \geq 3$ vanish. The three- and four-point couplings are then given by

$$\Gamma^{(3)}(0) = \Gamma^{(4)}(0)\phi_0, \qquad \lambda_2 = \Gamma^{(4)}(0). \tag{37}$$

With Eq. (30), we can express the minimum of the effective potential in terms of the curvature mass and λ_2, yielding

$$\phi_0^2 = \frac{3m^2_{\mathrm{curv}}}{\Gamma^{(4)}(0)}. \tag{38}$$

Using (38), the three-point function is expressed in terms of the full two- and four-point functions at vanishing momentum,

$$\Gamma^{(3)}(0) = \sqrt{3\Gamma^{(4)}(0)}m_{\mathrm{curv}}. \tag{39}$$

Evidently, in the classical limit with $Z_\phi = 1$ and $\tilde{\rho}_k = 0$, the curvature mass agrees with the pole mass. This limit is approached for asymptotically large pole masses, where the effective coupling $\lambda_\phi/m_{\mathrm{pole}}$ tends toward zero. Hence, the ultraviolet effective potential $V_{\mathrm{UV}}(\phi)$ with $k = \Lambda \to \infty$ is augmented with a classical dispersion with $\mu = -\Lambda^2$ and the initial (classical) coupling $\lambda_2 = \lambda_\phi$:

$$V_{\mathrm{UV}}(\phi) = \frac{1}{4!}\lambda_\phi(\phi^2 - \phi_0^2)^2, \qquad \phi_0^2 = \frac{6\Lambda^2}{\lambda_\phi}, \tag{40}$$

for $\phi^2 \geq \phi_0^2$. The initial curvature and pole mass are given by

$$m^2_{\mathrm{pole}} = m^2_{\mathrm{curv}} = 2\Lambda^2. \tag{41}$$

With these approximations, the real-time flow of the two-point function in the broken phase, derived in Appendix B, reads

$$\begin{aligned}
\partial_t\Gamma^{(2)}(\omega_+^2) = \dot{\mathcal{R}}\left(D_{\mathrm{pol}}(\omega_+^2) - \frac{1}{2}D^{\mathrm{dyn}}_{\mathrm{tad}}(\omega_+^2)\right) \\
+ AD_{\mathrm{fish}}(\omega_+^2) + 4k^2 - \partial_t\hat{S}^{(2)}_{\mathrm{ct}}.
\end{aligned} \tag{42}$$

The prefactors are given in Eq. (B6), and $\hat{S}^{(2)}_{\mathrm{ct}}$ is given by

$$\hat{S}^{(2)}_{\mathrm{ct}} = \mathrm{diagrams}(p^2 = -2k^2). \tag{43}$$

In addition to the polarization topology, we note that the flow equation in the broken phase differs from that in the symmetric phase. The constant part of Eq. (42) carries an additional factor of 2. This resembles the additional factor 2

of the squared pole mass in the broken phase compared to its symmetric-phase counterpart. Also, the prefactor of the tadpole diagram deviates from the symmetric case, since it includes the implicit k dependence of the internal lines via the flowing physical minimum.

C. Resumé

In both phases, we have a positive-curvature mass $m_{\mathrm{curv}} > 0$ on the equation of motion ϕ_0. Its value is related to the pole mass $m_{\mathrm{pole}} = k$ in the symmetric phase, and to $m_{\mathrm{pole}} = 2k$ in the broken phase. The difference between the flows is the existence of vertices $\Gamma^{(2n+1)}$ in the broken phase. They are proportional to sums of powers of ϕ_0—see (36)—and hence vanish in the symmetric phase. Specifically, the flow of the two-point function in the broken phase contains the diagrammatic topology of a vacuum polarization; see Fig. 7.

This leads us to the following structure: the CS flows are initiated deep in the symmetric and deep in the broken phase for large pole masses and a given classical coupling λ_ϕ; see Eqs. (32) and (40), respectively. For the broken phase, this entails that the field expectation value at the initial scale is also large as it scales with Λ; see Eqs. (38) and (40). Then, the pole mass is successively lowered, and for $k = 0$, one reaches the phase transition point from both sides. In particular, the flows do not leave the broken or symmetric phases. This is in seeming contradiction to the standard fRG picture in a scalar theory, where flows in the broken phase may end up in the symmetric phase, while those in the symmetric phase end up deeper in the symmetric phase. This apparent contradiction is resolved by the fact that ϕ_0 in the standard fRG is defined from the subtracted EOM. There, the trivial cutoff flow, which is $\propto k^2\phi^2$, is subtracted from the effective potential, and one recovers physics only in the limit $k \to 0$.

V. RESULTS

In this section, we present results for the spectral functions of the scalar propagator in the symmetric and broken phases. The discussion of the numerical implementation is deferred to Appendix E. The results allow for an investigation of the scattering processes in both phases. The present results are in remarkable quantitative agreement with those obtained with the spectral DSE in [1]. This agreement of the spectral functions from these two different functional approaches holds true for a large range of effective couplings λ_ϕ/m_ϕ; see Fig. 10(a). In this coupling regime, this agreement provides a nontrivial reliability check for both functional approaches, thus decreasing the respective systematic error. This error analysis is augmented with a comparison of the present advanced truncation with the classical vertex approximation in Appendix D.

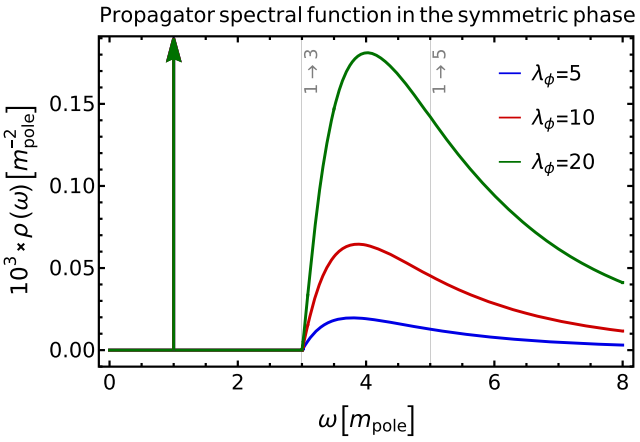

FIG. 9. Spectral functions for vanishing field value as a function of the frequency. All quantities are measured in units of the pole mass. $1 \to 3$ and $1 \to 5$ onsets are indicated in gray.

A. Symmetric phase

In the symmetric phase with $\phi_0 = 0$, we are left with the tadpole diagram in the flow of the two-point function (15). The resummation (27) introduces a nontrivial momentum dependence to the four-point function and, in consequence, also to the tadpole diagram. This allows us to calculate the propagator spectral function in the symmetric phase, i.e., at vanishing field value, where the polarization diagram is absent. For the respective flow equation on the real frequency axes, see (33). The resulting spectral function is shown in Fig. 9. In the symmetric phase, the scattering continuum starts at $3m_{\mathrm{pole}}$. As mentioned above, the dynamic tadpole contribution Eq. (A4) carries the momentum structure of the polarization diagram, resembling the s-channel structure of the four-vertex. Still, the onset of its imaginary part is at thrice the pole mass, since the bubble resummed vertex represents a series of $2 \to 2$ scatterings which leads to a generic two-particle onset of ρ_4. The quantum corrections to the symmetric phase propagator are small compared to those for the broken phase. The amplitude on the mass pole is close to 1 compared to the respective values in the broken phase; see Table I. This is expected, since the first dynamic contribution is of two-loop order and corresponds to the sunset topology. In the scaling limit, characterized by $\lambda_\phi/m_{\mathrm{pole}} \to \infty$, the amplitude of the mass pole decreases and the spectral weight is transferred to the scattering tail, which approaches a scaling form. While this limit goes beyond the scope of

TABLE I. Amplitudes $1/Z_\phi$ of the pole contribution for given effective couplings, corresponding to the scattering tails displayed in Figs. 10(a) and 9.

$\lambda_\phi/m_{\mathrm{pole}}$	$1/Z_\phi$ (fRG)	$1/Z_\phi$ (DSE)	$1/Z_\phi(\phi_0 = 0)$
5	0.971	0.969	0.9998
10	0.950	0.945	0.9995
20	0.921	0.907	0.9986

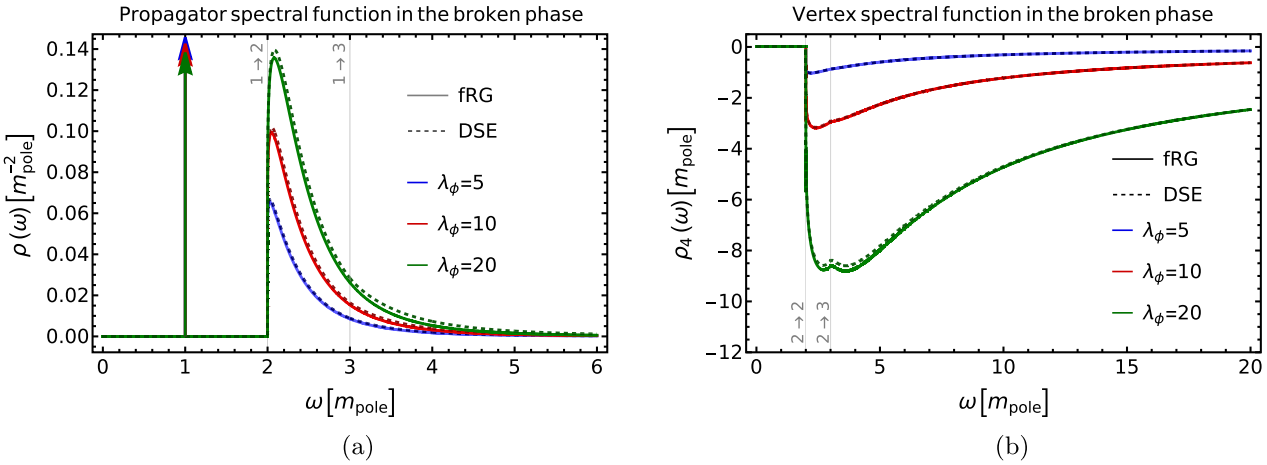

FIG. 10. Spectral functions as a function of Minkowski frequency in comparison to DSE results from [1]. In contrast to Fig. 2, all quantities are measured in units of the pole mass to facilitate the comparison with the DSE results. (a) Spectral function of the propagator. The $1 \to 2$ and $1 \to 3$ particle scattering onsets are indicated in gray. (b) Spectral function of the four-point function. The $2 \to 2$ and $2 \to 3$ particle scattering onsets are indicated in gray.

the present work, a full analysis of this regime is carried out in [41].

B. Broken phase

In the broken phase, the condensate is nonvanishing, $\phi_0 \neq 0$. To compute the spectral function, the flow equation is evaluated on the real frequency axes; see Eq. (42).

The N-particle onset positions of the spectral scattering tail are governed by the imaginary part of (12). For the polarization diagrams, where only propagators come into play, the flow exhibits an onset at the sum of the two mass poles. In contrast, the contribution of the tadpole leads to an onset at thrice the pole mass, as the four-point spectral function only consists of a scattering continuum starting at $2m_{\rm pole}$, cf. Fig. 10(b). A more detailed discussion of the scattering onsets in general is found in Appendix F, and one specifically for the tadpole in Sec. V A.

In Fig. 10(a), the spectral function from the current fRG approach is compared to spectral DSE results from [1]. Every quantity is measured relative to the respective pole mass to facilitate comparison with the DSE results. This allows us to compare the relative magnitude of the scattering continua for different coupling strengths. For effective couplings $\lambda_\phi/m_{\rm pole} \lesssim 20$, the spectral weight of the scattering continuum is subleading, as can be inferred from the combination of Fig. 2(b) and the sum rule (5). The amplitudes of the pole contributions are listed in Table I.

We find a remarkable agreement of both methods in the tested coupling range. For effective couplings $\lambda_\phi/m_{\rm pole} \approx 20$, the deviations start growing, specifically at the thresholds. Deviations between both methods arise due to differences in the resummation structure of the two functional equations in the current truncation. The convergence of functional techniques for a large range of couplings is nontrivial and strengthens our confidence in spectral functional approaches.

In general, the tail of the propagator spectral function is enhanced for stronger couplings, while the residue of the mass pole decreases as the scattering states become more accessible due to the rising dimensionless interaction strength. The three- and higher-N-particle onsets are graphically not visible in the full spectral functions of Fig. 10(a), but they are present in the data. In the limit of large couplings, we expect the three-particle onset to become more pronounced as the tadpole contribution becomes large.

The four-point spectral function shown in Fig. 10(b) consists of only a negative scattering tail, corresponding to a $2 \to 2$ scattering process. For higher couplings, the three-particle onset becomes visible. The different suppression of higher-N-particle thresholds in the propagator and four-point spectra are explained by dimensional analysis. While for the propagator spectral function, higher-N-particle onsets are suppressed by their squared energy threshold,

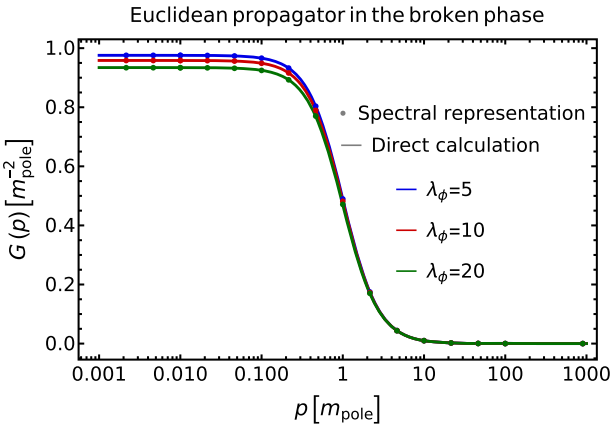

FIG. 11. Propagator as a function of Euclidean frequency. This result serves as a cross-check between a direct computation via the flow and a calculation using the spectral functions.

the four-point spectral function decays only with λ^{-1}, leading to a suppression linear in their respective energy thresholds. In both cases, four-particle or higher onsets are strongly suppressed, since they come with at least one additional loop each.

Figure 11 shows the Euclidean propagators corresponding to the spectral functions of Fig. 10(a). As a cross-check, we compare the Euclidean propagator calculated from the spectral representation to the propagator directly obtained from the integrated Euclidean flow. We find the spectral representation to hold.

VI. CONCLUSION

In the present work, we computed single-particle spectral functions of a scalar ϕ^4-theory within the spectral functional renormalization group approach, put forward in [8]. This approach leads to renormalized spectral flows with flowing renormalization, and it facilitates a fully self-consistent computation of spectral functions. We derived full flow equations for the inverse propagator in both the symmetric and broken regimes of the theory; for a detailed discussion, see Secs. III C and IV C.

Our setup is manifestly Lorentz invariant and sustains the causal properties of the theory throughout the flow. Every point on the Callan-Symanzik RG trajectory is a physical theory of scale k. Trajectories in the symmetric and broken regimes each start from an infinitely heavy theory in the respective phase and meet at the phase boundary in the strongly interacting massless limit of the theory; see Sec. III A and Fig. 3. Thereby, our setup avoids flows through the strongly interacting phase transition regime, which are usually present in momentum cutoff flows. This minimizes the systematic error stemming from the strong dynamics in the vicinity of a phase transition, where the flows are highly sensitive to truncation artefacts. Furthermore, the implementation of a flowing renormalization condition eliminates the need of fine-tuned initial conditions and allows for monotonic mass flows.

The explicit results in the broken phase are in impressive agreement with those obtained in [1] within the spectral DSE; see Sec. V B. This affirms the reliability of the spectral functional approach for the computation of fundamental Minkowski spacetime correlation functions.

In contrast to DSE, the fRG approach captures average momentum dependencies of vertices via their scale dependence. This allows us to include nontrivial vertex dynamics without resorting to intricate spectral representations of higher correlation functions. Furthermore, the current spectral fRG approach is straightforwardly and easily extended to include the flow of the full effective potential. This work represents an important step toward unraveling real-time correlations in QCD from first principles with spectral functional approaches. We hope to report on respective results in the near future.

ACKNOWLEDGMENTS

We thank Gernot Eichmann, Manuel Reichert, Johannes Roth, and Lorenz von Smekal for discussions and collaborations on related projects. This work is done within the fQCD Collaboration [42], and we thank its members for discussion and collaborations on related projects. This work is funded by the Deutsche Forschungsgemeinschaft (DFG, German Research Foundation) under Germany's Excellence Strategy No. EXC 2181/1–390900948 (the Heidelberg STRUCTURES Excellence Cluster) and under the Collaborative Research Centre SFB No. 1225 (ISOQUANT). J. H. and F. I. acknowledge support by the Studienstiftung des deutschen Volkes. N. W. is supported by the Hessian collaborative research cluster ELEMENTS and by the DFG Collaborative Research Centre CRC-TR 211 (Strong-interaction matter under extreme conditions).

APPENDIX A: SPECTRAL DIAGRAMS

The general spectral form of the diagrams in Figs. 5 and 6 is given by

$$\begin{aligned} D_{\mathrm{tad}}(p^2) &= \left(\prod_{i=1}^{2}\int_{\lambda_i}\rho(\lambda_i)\right)\mathcal{L}_{\mathrm{tad}}(\vec{\lambda},p^2),\\ D_{\mathrm{pol}}(p^2) &= \left(\prod_{i=1}^{3}\int_{\lambda_i}\rho(\lambda_i)\right)\mathcal{L}_{\mathrm{pol}}(\vec{\lambda},p^2),\\ D_{\mathrm{fish}}(p^2) &= \left(\prod_{i=1}^{2}\int_{\lambda_i}\rho(\lambda_i)\right)\mathcal{L}_{\mathrm{fish}}(\vec{\lambda},p^2), \end{aligned} \tag{A1}$$

with $\vec{\lambda}=(\lambda_1,\ldots,\lambda_n)$ denoting the ordered vector of spectral masses. The loop structure reads

$$\begin{aligned} \mathcal{L}_{\mathrm{tad}}(\vec{\lambda},p^2) &= \int_q \frac{\Gamma^{(4)}[p,q,-p]}{(q^2+\lambda_1^2)(q^2+\lambda_2^2)},\\ \mathcal{L}_{\mathrm{pol}}(\vec{\lambda},p^2) &= \int_q \frac{(\Gamma^{(3)}[p,q])^2}{(q^2+\lambda_1^2)(q^2+\lambda_2^2)((p-q)^2+\lambda_3^2)},\\ \mathcal{L}_{\mathrm{fish}}(\vec{\lambda},p^2) &= \int_q \frac{\Gamma^{(3)}[p,q]\Gamma^{(4)}[p,q,0]}{(q^2+\lambda_1^2)((p-q)^2+\lambda_2^2)}, \end{aligned} \tag{A2}$$

where the vertex functions are not specified yet, and we have dropped the field argument for readability. With the approximations discussed in Sec. IV, we have fixed all correlation functions, and we can compute the final expressions for the diagrams. For the fish diagram, the four-point function is connected to the constant scale derivative of the field. With (39) and (37), the polarization and fish diagrams of the flow equation in the broken phase read

$$D_{\mathrm{pol}}[p^2] = (\Gamma^{(3)})^2 \int_{\vec{\lambda}} \rho(\lambda_1)\rho(\lambda_2)\rho(\lambda_3) I_{\mathrm{pol}}(\vec{\lambda}, p^2),$$
$$D_{\mathrm{fish}}[p^2] = \frac{(\Gamma^{(3)})^2}{\phi_0} \int_{\vec{\lambda}} \rho(\lambda_1)\rho(\lambda_2) \tilde{I}_{\mathrm{pol}}(\vec{\lambda}, p^2), \tag{A3a}$$

where

$$I_{\mathrm{pol}}(\vec{\lambda}, p^2) = \int_q \frac{1}{(q^2+\lambda_1^2)(q^2+\lambda_2^2)((q-p)^2+\lambda_3^2)},$$
$$\tilde{I}_{\mathrm{pol}}(\vec{\lambda}, p^2) = \int_q \frac{1}{(q^2+\lambda_1^2)((q-p)^2+\lambda_2^2)}, \tag{A3b}$$

and $\vec{\lambda}$ is the ordered vector of spectral parameters, one for each internal propagator in the diagram. We denoted the loop structure of the fish diagram as $\tilde{I}_{\mathrm{pol}}$, since it carries the momentum structure of a DSE polarization diagram. The loop integrals I and $\tilde{I}$ are evaluated analytically and given in terms of real and imaginary frequencies in Appendix F.

Substituting the four-vertex in (15) with the respective spectral representation (6), the constant classical part of the tadpole diagram is absorbed by renormalization. The remaining dynamical part of the tadpole diagram reads

$$D^{\mathrm{dyn}}_{\mathrm{tad}}(p) = \int_{\vec{\lambda}} \rho(\lambda_1)\rho(\lambda_2)\rho_4(\lambda_3) I_{\mathrm{pol}}(\vec{\lambda}, p^2). \tag{A4}$$

The four-point spectral function ρ_4 (A4) is obtained from (27) in both phases. As discussed below Eq. (27), there are further diagrams with two or four three-point functions contributing to ρ_4. These diagrams are suppressed by roughly an order of magnitude.

APPENDIX B: RENORMALIZED FLOW OF THE TWO-POINT FUNCTION ON THE PHYSICAL MINIMUM

In this appendix, we provide details on the derivation of the flow equation in the broken phase Eq. (25a). In particular, we explain the crucial role of the three-point function in (22) for obtaining one-loop perturbation theory as leading-order behavior. We show that the flow of the two-point function has the expected sign [see (23)], if we include the flow of the minimum correctly, and that the on-shell renormalization condition (20) can be imposed consistently.

The flow equation in the broken phase reads

$$\frac{d}{dt}\Gamma^{(2)}[\phi_0](p) = (\partial_t\phi_0) S^{(3)}[\phi_0] - (2-\eta_\phi) Z_\phi k^2 + \dot{\mathcal{R}}\left[-\frac{1}{2}D_{\mathrm{tad}} + D_{\mathrm{pol}}\right] - \partial_t\phi_0 D_{\mathrm{fish}} - \partial_t S_{\mathrm{ct}}[\phi_0], \tag{B1a}$$

where

$$\dot{\mathcal{R}} = (\partial_t\phi_0\Gamma^{(3)}[\phi_0] - (2-\eta_\phi) Z_\phi k^2), \tag{B1b}$$

as derived in Sec. III C.

To renormalize the flow of the two-point function and show how the correct sign of the flow is recovered by the inclusion of $\partial_t\phi_0$, we first separate the tree-level and loop-induced running of the prefactors of the diagrams in Eq. (B1a). To that end, we start with the full three-point function in (B1b). The separation into trivial and loop-induced RG running can be made apparent by introducing a corresponding split of the curvature mass (30) via $\Delta m^2_{\mathrm{curv}} = m^2_{\mathrm{curv}} - 2Z_\phi k^2$:

$$\partial_t\phi_0\Gamma^{(3)} = \frac{1}{2}(\partial_t\phi_0^2)\Gamma^{(4)} = \frac{3}{2}\left(\partial_t\Delta m^2_{\mathrm{curv}} + 2Z_\phi(2-\eta_\phi)k^2 - m^2_{\mathrm{curv}}\frac{\partial_t\Gamma^{(4)}}{\Gamma^{(4)}}\right). \tag{B2a}$$

In the first line, we related the three- and four-point functions by (37), and we used (38) in the second step.

For the classical three-vertex in (B1a), we analogously obtain

$$\partial_t\phi_0 S^{(3)} = \frac{\lambda_\phi}{\Gamma^{(4)}}(\partial_t\phi_0\Gamma^{(3)}). \tag{B2b}$$

With (A3a), the fish diagram in (B1a) carries a prefactor proportional to

$$\frac{\partial_t\phi_0}{\phi_0} = \frac{\partial_t m^2_{\mathrm{curv}}}{m^2_{\mathrm{curv}}} - \frac{\partial_t\Gamma^{(4)}}{\Gamma^{(4)}}. \tag{B3}$$

Inserting (B2) and (B3) into Eq. (B1a), we can write down the final flow equation for the two-point function in the broken phase:

$$\frac{d}{dt}\Gamma^{(2)}[\phi_0](p) = \dot{\mathcal{R}}\left(-\frac{1}{2}D_{\mathrm{tad}} + D_{\mathrm{pol}}\right) + AD_{\mathrm{fish}} + B(2-\eta_\phi)Z_\phi k^2 + C - \partial_t S^{(2)}_{\mathrm{ct}}, \tag{B4a}$$

with

$$\dot{\mathcal{R}} = 2Z_\phi(2-\eta_\phi)k^2 + \frac{3}{2}m^2_{\mathrm{curv}}\left(\frac{\partial_t\Delta m^2_{\mathrm{curv}}}{m^2_{\mathrm{curv}}} - \frac{\partial_t\Gamma^{(4)}}{\Gamma^{(4)}}\right),$$
$$A = -\frac{\phi_0}{2}\left(\frac{\partial_t m^2_{\mathrm{curv}}}{m^2_{\mathrm{curv}}} - \frac{\partial_t\Gamma^{(4)}}{\Gamma^{(4)}}\right),$$
$$B = \left(\frac{3\lambda_\phi}{\Gamma^{(4)}} - 1\right),$$
$$C = \frac{3}{2}m^2_{\mathrm{curv}}\frac{\lambda_\phi}{\Gamma^{(4)}}\left(\frac{\partial_t\Delta m^2_{\mathrm{curv}}}{m^2_{\mathrm{curv}}} - \frac{\partial_t\Gamma^{(4)}}{\Gamma^{(4)}}\right). \tag{B4b}$$

The diagrams $D_{\rm pol}$, $D_{\rm fish}$ and $D^{\rm dyn}_{\rm tad}$ are given in Eqs. (A3) and (A4), respectively.

The prefactor of the first term in (B4b), $\dot{\mathcal{R}}$, carries the scale dependence of the internal propagators on the physical minimum. It takes the role of the regulator derivative in usual fRG applications. The first term of $\dot{\mathcal{R}}$ and the third term of the flow in (B4a) are explicitly proportional to k^2, and they have the same structure as the respective contributions in (15), where the flow equation is evaluated at arbitrary values of the field. However, it carries an additional relative factor -2, stemming from the three-point function, which is proportional to $\partial_t\phi_0\Gamma^{(3)}$. In total, the tree-level term of $\dot{\mathcal{R}}$ is positive and can be written as the t-derivative of $2Z_\phi k^2$. This reflects the positivity of the physical pole mass. At one-loop order, it reduces to $4k^2$, resembling the k dependence of a classical propagator with $m_\phi = 2k^2$; see Eq. (23).

The same holds true for the constant part of the flow, given by the third and fourth terms of (B4a). Complementary to $\dot{\mathcal{R}}$, these encode the explicit running of the mass. At tree level, this running reduces to $4k^2$, which is simply the flow of the classical (squared) mass on the physical minimum. Hence, the deviation of the constant part of the flow from the classical running is, as expected, of one-loop order and beyond, and it can be absorbed in the renormalization constant. With that, we can consistently impose our renormalization condition.

The second term of (B4a) is proportional to the fish diagram. Note that $D_{\rm fish}$ carries a factor $1/\phi_0$, which cancels the respective factor in A. At one-loop order, it carries the running of the classical three-point function. Together, $D_{\rm fish}$ and $D_{\rm pol}$ can be written as the total derivative of the (one-loop) vacuum polarization.

We now apply our renormalization condition (20) to the flow (B4a), for which it translates into the condition

$$\partial_t m^2_{\rm pole} = 4k^2. \tag{B5}$$

This specifies our counterterm flow and leads us to the final renormalized flow equation in the broken phase:

$$\frac{d}{dt}\Gamma^{(2)}(p) = \dot{\mathcal{R}}\left(D_{\rm pol}(p) - \frac{1}{2}D^{\rm dyn}_{\rm tad}(p)\right) + AD_{\rm fish}(p) + 4k^2 - \partial_t\hat{S}^{(2)}_{\rm ct}, \tag{B6}$$

where we have split the tadpole into a constant and a dynamical p-dependent part defined by (A4), via the spectral representation Eq. (6) of the four-vertex. Furthermore, we have dropped all constants in p of order $(\lambda_\phi k)$, including the constant part of the tadpole, as they are subtracted by the renormalization constant implicitly specified by Eq. (B5). The remaining $\partial_t\hat{S}^{(2)}_{\rm ct}[\phi_0]$ now comprises only the counterterms of the diagrammatic contributions, where the renormalization scale is the pole mass.

APPENDIX C: FLOW OF ϕ_0 AND CRITICAL EXPONENTS

In this appendix, we discuss the evolution of the solution of the EOM, ϕ_0, in the broken phase. It is given by Eq. (38). This exact relation depends on λ_2, which we have identified with $\Gamma^{(4)}$, dropping higher-order terms proportional to λ_3, λ_4, and ϕ_0 itself. Implicitly, these terms can be included by solving the flow of ϕ_0. It is derived from the EOM for constant fields, which is solved for a k-dependent ϕ_0. Acting with a total t-derivative on the EoM (16) leads us to

$$\partial_t\phi_0 = -\frac{\partial_t V^{(1)}_{\rm eff}(\phi_0)}{V^{(2)}_{\rm eff}(\phi_0)} = -\frac{\partial_t V^{(1)}_{\rm eff}(\phi_0)}{m^2_{\rm curv}}. \tag{C1}$$

The denominator is simply the curvature mass squared, while the numerator is given by the first field derivative of the CS equation (14), evaluated at ϕ_0. At each flow step, the latter generates higher-order terms beyond the approximation in Eq. (26). In summary, if we are using the flow equation in (C1), we implicitly take into account terms dropped in (38). In the present approximation, the numerator of (C1) reads

$$\partial_t V^{(1)}[\phi_0] = \phi_0(2-\eta_\phi)Z_\phi k^2\left[\frac{1}{2}D_{\rm tad}(0) - 1\right] - \phi_0(\partial_t\Delta m^2). \tag{C2}$$

The last term stems from the flow of the counterterm action

$$\partial_t S_{\rm ct}[\phi] = {\rm Tr}\,\frac{1}{2}(\partial_t\Delta m^2)\phi^2. \tag{C3}$$

Collecting the terms proportional to ϕ_0 and $\partial_t\phi_0$, we arrive at

$$\partial_t\log(\phi_0) = \frac{(2-\eta_\phi)Z_\phi k^2}{m^2_{\rm curv}}(1+\mathcal{T}), \tag{C4}$$

where $\mathcal{T}$ comprises the corrections from the tadpole diagram and the counterterm

$$\mathcal{T} = -\frac{1}{2}D_{\rm tad}(0) + \frac{\partial_t\Delta m^2}{(2-\eta_\phi)Z_\phi k^2}. \tag{C5}$$

Equation (C4) is easily integrated, leading to

$$\phi_0 = \phi_{0,\Lambda}\exp\left\{\int_\Lambda^k \frac{dk}{k}\frac{(2-\eta_\phi)Z_\phi k^2}{m^2_{\rm curv}}(1+\mathcal{T})\right\}, \tag{C6}$$

where $\phi_{0,\Lambda}$ is the classical ultraviolet value of the condensate in the initial UV effective potential Eq. (40) at the

initial large mass Λ. For smaller pole masses, the condensate gets progressively smaller and vanishes for $k = 0$. We can simplify (C6) further by noting that the squared curvature mass—see (38)—is conveniently written in terms of the spectral representation

$$m^2_{\text{curv}} = \frac{2Z_\phi k^2}{1 + \int_2^\infty \frac{d\lambda}{\lambda}\bar{\rho}(\lambda)}, \tag{C7}$$

where we define the RG-invariant spectral function as

$$\bar{\rho}(\lambda) = \frac{2Z_\phi k^2}{\pi}\rho(\sqrt{2k^2}\lambda). \tag{C8}$$

With (C7), the exponent of (C6) reads

$$\int_\Lambda^k \frac{dk}{k}\left[\left(1 - \frac{\eta_\phi}{2}\right)\left(1 + \int_2^\infty \frac{d\lambda}{\lambda}\bar{\rho}(\lambda)\right)(1 + \mathcal{T})\right]. \tag{C9}$$

For large k (i.e., $\lambda_\phi \ll k$), we can approximate $m^2_{\text{curv}} \approx 2k^2$, and $\lambda_2 = \Gamma^{(4)}(0) \approx \lambda_\phi$. The flow of the renormalization constants is dominated by the tadpole contribution for large cutoff scales. It is of mass dimension 2, and at leading order in k it is proportional to $(\lambda_\phi k)$. Consequently, $\frac{\partial_t \Delta m^2}{k^2} \approx 0$, along with the tadpole contribution

$$D_{\text{tad}} = \lambda_\phi \int \frac{d^3q}{(2\pi)^3}\frac{1}{(q^2 + 2k^2)^2} = \frac{\lambda_\phi}{\sqrt{2}k8\pi}. \tag{C10}$$

The propagator is then well approximated by the free one, $Z_\phi = 1$ and $\tilde{\rho} = 0$, and Eq. (C9) reduces to $1 + \mathcal{T} \approx 1 + \bar{\lambda}_\phi c$, with the effective coupling $\bar{\lambda}_\phi = \lambda_\phi/k$ and a dimensionless constant c. In the limit of large masses, (C11) flows to the classical solution as expected:

$$\phi_{0,k} = \phi_{0,\Lambda}\exp\left\{\int_\Lambda^k \frac{dk}{k} + c\int_\Lambda^k \frac{dk}{k}\bar{\lambda}\right\} \longrightarrow \phi_{0,\Lambda}\left(\frac{k}{\Lambda}\right). \tag{C11}$$

Similar equations could be formulated in terms of $\rho = \phi^2$, reflecting the symmetry of the theory. In $O(N)$ theories and in the real scalar case, such a representation is typically used, as derivatives in ρ project directly on λ_n in both phases. While all different formulations are equivalent if the full effective potential is used, they deal differently with the approximation in Eq. (26).

1. Phase transition and critical scaling

Here we provide a qualitative discussion on the scaling limit and use the integrated flow of the physical minimum, ϕ_0, and the (hyper)scaling relation (C12) to derive explicit equations for the scaling exponent η_ϕ. The phase transition between the symmetric and broken phases is reached with $k \to 0$ in both phases. In the limit of a vanishing pole mass, $m^2_{\text{pole}} = 2k^2 = 2|\mu| \to 0$, we are interested in the running of the "magnetization," $\bar{\phi}_0 = \phi_0/\sqrt{Z_\phi}$. The division by $1/\sqrt{Z_\phi}$ eliminates the RG scaling of the expectation value and leads to the physical observable. In the scaling limit, the magnetization acquires a scaling form

$$\bar{\phi}_0 \propto \tau^\beta, \qquad \beta = \frac{1}{2}\nu(1 + \eta_\phi) \approx 0.3264, \tag{C12}$$

where $\nu \approx 0.6300$ and $\eta_\phi \approx 0.03630$ are the scaling exponents of the three-dimensional Ising universality class. The tuning parameter τ is, in contrast to usual critical theory, not directly proportional to the mass parameter μ or k^2 as a consequence of the flowing on-shell renormalization. To see that, we consider the scaling form of the correlation length

$$\xi \propto \tau^{-\nu}, \tag{C13}$$

with the mean-field scaling $\nu = \frac{1}{2}$. In general, the correlation length is inversely proportional to the lowest-lying pole of the propagator. Beyond the mean field theory, the correlation length acquires an anomalous scaling in dimensions below $d = 4$. With the on-shell renormalization procedure, this anomalous scaling is hidden, and we have

$$\xi \propto k^{-1} \tag{C14}$$

for all cutoff scales. This entails that the tuning parameter τ is related to the pole mass $m_{\text{pole}} \propto k$ as

$$\tau \propto k^{\frac{1}{\nu}}. \tag{C15}$$

In every flow step, the diagrams of the flow introduce an anomalous scaling to the pole mass, which is subtracted by the counterterm and expresses the renormalization of the full scaling of the pole mass to the classical one. Hence, the scaling exponent ν is encoded in the flow of the counterterm in the scaling limit. With (C15), the magnetization (C12) can be rewritten as

$$\bar{\phi}_0 \propto k^{\frac{\beta}{\nu}}, \qquad \frac{\beta}{\nu} = \frac{1}{2}(1 + \eta_\phi). \tag{C16}$$

The k scaling of the magnetization is encoded in the $k \to 0$ limit of Eq. (C6). Resolving the brackets, we notice that the first two terms of the exponent (C9) can be integrated immediately, leading to

$$\phi_0 = \phi_{0,\Lambda}\sqrt{Z_\phi}\left(\frac{k}{\Lambda}\right)\exp\left\{\int_\Lambda^k \frac{dk'}{k'}\mathcal{D}(k')\right\}, \tag{C17a}$$

where we have used the definition of η_ϕ. The residual integrand is abbreviated as

$$\mathcal{D}(k) = \left(1 - \frac{\eta_\phi}{2}\right)\left[(1+\mathcal{T})\int_2^\infty \frac{d\lambda}{\lambda}\bar{\rho}(\lambda) + \mathcal{T}\left(1 + \int_2^\infty \frac{d\lambda}{\lambda}\bar{\rho}(\lambda)\right)\right], \tag{C17b}$$

with $\mathcal{T}$ given in (C5). In the scaling regime, we have $k \to 0$ and

$$\bar{\phi}_0 \propto \lim_{k\to 0} k \exp\left\{\int_\Lambda^k \frac{dk'}{k'}\mathcal{D}(k')\right\}. \tag{C18}$$

In the limit $k \to 0$, the integral in Eq. (C18) diverges logarithmically with the prefactor $\mathcal{D}_0 = \mathcal{D}(0)$. This allows to identify β/ν with $\mathcal{D}_0$ and solve (C16) for η_ϕ:

$$\eta_\phi = 1 + 2\mathcal{D}_0. \tag{C19}$$

The prefactor $\mathcal{D}_0$ is either computed for $k \to 0$ or is extrapolated when the scaling regime is reached. Alternatively, η_ϕ can be computed directly from the flow in the scaling limit via its definition; see Eq. (E10c). The size of the scaling regime can be estimated from the running of the four-point function: For large values of the dimensionless coupling $\lambda_\phi/m_{\rm pole} \gg 1$, the loop correction in the denominator of Eq. (27) outgrows the constant part,

$$\Gamma^{(4)}(p) = \frac{\lambda_\phi}{1 + \frac{\lambda_\phi}{2}\int_q G(p+q)G(q)} \to \frac{2}{\int_q G(p+q)G(q)}, \tag{C20}$$

and the flow becomes independent of the coupling. Our computational setup did not allow for a direct computation in this limit. Hence, we refrain from giving an estimate for the scaling exponents and defer quantitative results to future publications.

Let us close this investigation with a discussion of the spectral function in the critical regime. To begin with, for $k \to 0$, the pole contribution of the propagator vanishes as $Z_\phi \propto k^{-\eta_\phi} \to \infty$. In turn, for $k = 0$, the scattering tail carries all the weight, and the solution for $k = 0$ is given by

$$\tilde{\rho}(\lambda) \propto \frac{1}{\lambda^{2(1-\frac{\eta_\phi}{2})}} \quad \to \quad G_k(p) \propto \frac{1}{(p^2)^{(1-\frac{\eta_\phi}{2})}}. \tag{C21}$$

Note that the scaling in (C21) is naturally cut off in the infrared at $\lambda = 2m_{\rm pole}$ according to (21). In the ultraviolet, for $\lambda \to \infty$, the spectral function also has to decay faster than (C21). As has been discussed in [2,43], the propagators of *physical* states or fields have to decay as $1/p^2$ for large momenta. This is at odds with (C21), and indeed the spectral function $\tilde{\rho}$ in (C21) is not (UV) normalizable. For a finite k, $\tilde{\rho}$ decays faster than $1/\lambda^2$, as is manifest in our explicit solutions in the broken and symmetric phases, Figs. 9 and 10(a), respectively.

APPENDIX D: VARYING THE TRUNCATION

This section is dedicated to the comparison of our approximation to the classical vertex approximation. The latter is given by

$$\Gamma^{(4)} = \lambda_\phi, \qquad \Gamma^{(3)} = \sqrt{3\lambda_\phi} m_{\rm curv}. \tag{D1}$$

The value of the tadpole diagram is absorbed in the renormalization constant, and the only remaining

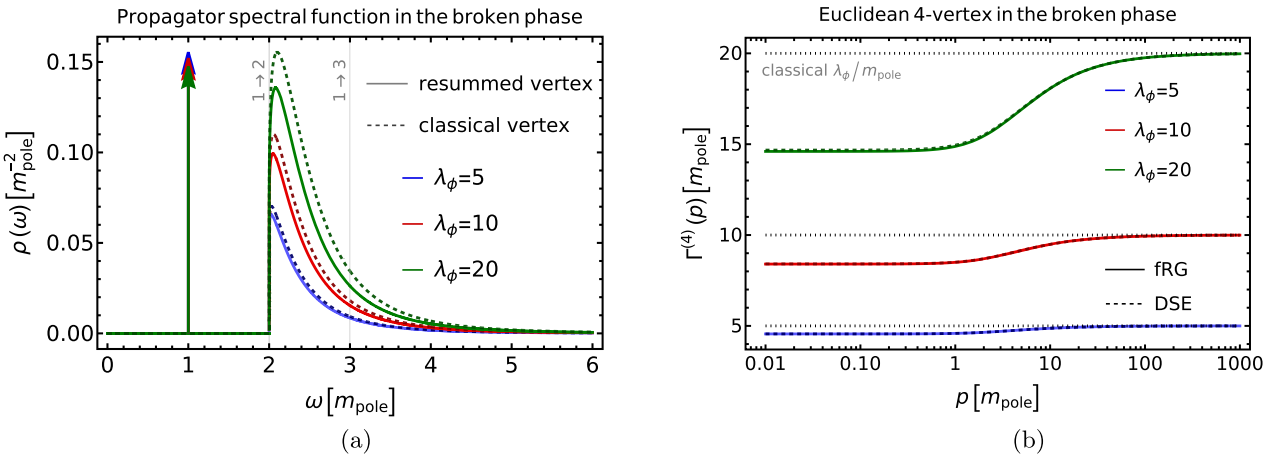

FIG. 12. Propagator spectral functions and Euclidean four-point functions in the broken phase. All quantities are measured in units of the pole mass. (a) Comparison of the spectral functions within a classical vertex approximation to the results with a bubble resummed vertex function. Both spectral functions where calculated via the spectral fRG. (b) Four-point vertex as function of Euclidean frequency. Results are obtained from the respective spectral functions in Fig. 10(a). The classical values of the vertices are indicated in gray.

contribution is the polarization diagram in Eq. (F4). Note that this approximation leads to a nonzero scattering spectrum only, if evaluated in the broken phase with a finite three-point function.

The resulting spectral functions are presented in Fig. 12(a), indicated by dashed lines. All curves are measured in units of the respective pole masses to compare the magnitude of the scattering spectra with our main results. By introducing the resummed quantum corrections to the four-point function, its amplitude in the infrared is lowered due to the negativity of the respective scattering spectra; see Figs. 12(b) and 10(b). This leads to a systematic decrease of the spectral tail compared to the classical vertex approximation. Other than that, the visible structure is very similar. Nevertheless, the classical approximation misses any contribution of the tadpole and is quantitatively different from the result with a nontrivial four-point function for higher couplings in the broken phase. In the symmetric phase, however, the inclusion of the tadpole momentum structure is crucial to generating a nontrivial scattering spectrum with the fRG.

APPENDIX E: TECHNICAL DETAILS AND NUMERICS

This section is dedicated to the numerical solution of the flow equation. First, we rewrite the leading contributions as scale derivatives and integrate by parts in the k direction. This allows us to flow the nonanalyticities at the respective onset positions analytically; see Eq. (E2). We will make use of this relation to define consistent initial conditions in the UV. The second part of this appendix explains the numerical algorithm we used to obtain the results given in Sec. V.

1. Leading order and initial conditions

Inserting (21) into (A1), we find all combinations of poles and tails we have to integrate over. The leading order is given by the contribution of δ functions only and is already present on the classical level. To study the structure of the flow and the dependency of the result of the initial condition, we first note that certain contributions of the Callan-Symanzik flow can be rewritten in terms of a scale derivative. This is possible for every contribution to the Callan-Symanzik flow that carries only pole contributions on the two lines surrounding the (modified) regulator insertion in Fig. 7. This allows us to integrate the flow by parts, which reduces the degree of divergence of potential integrable singularities and simplifies the numerical treatment. To this end, we rewrite the (modified) fRG polarization diagram at leading order as

$$I_{\mathrm{pol}}(m_{\mathrm{pole}},m_{\mathrm{pole}},m_{\mathrm{pole}},p^2)=-\frac{1}{8k}\partial_k\tilde{I}_{\mathrm{pol}}(m_{\mathrm{pole}},m_{\mathrm{pole}},p^2), \tag{E1}$$

where the factor $1/4k$ follows from the k-derivative of the spectral kernel with $\partial_k m^2_{\mathrm{pole}}=4k$, and another factor $1/2$ accounts for the double-counting from hitting both arguments in k with the derivative. This connects both polarization-type momentum structures, I_{pol} and $\tilde{I}_{\mathrm{pol}}$, given in (A3b). Evaluating every spectral parameter on the mass pole, we can integrate the combined contribution of the polarization and fish diagrams to arrive at

$$\begin{aligned}[\Gamma^{(2)}(p^2)]^k_\Lambda&=\int_\Lambda^k\frac{dk}{k}\frac{(\Gamma_k^{(3)})^2}{Z_\phi^2}\left(-\frac{\dot{\mathcal{R}}}{8Z_\phi k}\partial_k+\frac{A}{\phi_0}\right)\tilde{I}_{\mathrm{pol}}(p^2)\\&=[-\mathcal{F}(k)\tilde{I}_{\mathrm{pol}}(p^2)]^k_\Lambda+\int_\Lambda^k\frac{dk}{k}\mathcal{L}(k)\tilde{I}_{\mathrm{pol}}(p^2),\end{aligned} \tag{E2}$$

where we have summarized the prefactors of the fRG polarization diagram and the prefactors from the t-integral as

$$\mathcal{F}(k)=\frac{\dot{\mathcal{R}}(\Gamma_k^{(3)})^2}{8Z_\phi^3k^2}=\left[\frac{(2-\eta_\phi)}{4}+\frac{\mathcal{S}}{Z_\phi}\right]\frac{(\Gamma_k^{(3)})^2}{Z_\phi^2}, \tag{E3}$$

with

$$\mathcal{S}=\frac{3}{16}\frac{m^2_{\mathrm{curv}}}{k^2}\left(\frac{\partial_t\Delta m^2_{\mathrm{curv}}}{m^2_{\mathrm{curv}}}+\frac{\partial_t\Gamma^{(4)}}{\Gamma^{(4)}}\right). \tag{E4}$$

The boundary term will be the leading contribution. At one-loop order (i.e., $Z_\phi=1$ and $\Gamma^{(4)}=\lambda_\phi$), $\mathcal{S}$ vanishes identically and $\mathcal{F}$ reduces to $\frac{1}{2}(S^{(3)})^2$, which is the prefactor of the one-loop polarization diagram times the squared classical three-vertex. The factor in the remaining integral reads

$$\begin{aligned}\mathcal{L}(k)&=\left(\partial_t\mathcal{F}(k)+\frac{A}{\phi_0}\frac{(\Gamma_k^{(3)})^2}{Z_\phi^2}\right)\\&=\left\{\frac{(2-\eta_\phi)}{4}\frac{\partial_t\Gamma^{(4)}}{\Gamma^{(4)}}-\frac{(2-\eta_\phi)}{2}\eta_\phi+\frac{\dot{\eta_\phi}}{4}-\frac{\eta_\phi\partial_t m^2_{\mathrm{curv}}}{4m^2_{\mathrm{curv}}}\right.\\&\quad\left.+\frac{1}{Z_\phi}\left[\partial_t\mathcal{S}+\mathcal{S}\left(3\eta_\phi+\frac{\partial_t m^2_{\mathrm{curv}}}{m^2_{\mathrm{curv}}}+\frac{\partial_t\Gamma^{(4)}}{\Gamma^{(4)}}\right)\right]\right\}\frac{(\Gamma_k^{(3)})^2}{Z_\phi^3},\end{aligned} \tag{E5}$$

where the tree-level terms stemming from $\mathcal{F}(k)$ and A cancel exactly. With that, we recover one-loop perturbation theory. Without the additional one-loop structure of the three-point function in Eq. (25a) (i.e., $A=0$), the remaining tree-level term would spoil the one-loop result.

To discuss the necessity of a consistent initial condition, it is instructive to work out the one-loop result from a spectral fRG perspective. In the large-k limit, we can neglect the nontrivial flow of $\Gamma^{(2)}(p=0)$ and Z_ϕ, leading

to $Z_\phi = 1$ and $(\Gamma_k^{(3)})^2 = 3\lambda m_{\text{pole}}^2$, with $m_{\text{pole}}^2 = 2k^2$. Equation (E2) is then readily integrated and reduces to

$$\Gamma^{(2)}_{\text{1-loop}}(p^2)|_k = \Gamma^{(2)}(p^2)|_\Lambda + 3\lambda_\phi [k^2 \tilde{I}_{\text{pol}}(\sqrt{2}k, \sqrt{2}k, p^2)]_k^\Lambda. \tag{E6}$$

With a classical initial condition, (E6) leads to

$$\Gamma^{(2)}_{\text{1-loop}}(p^2)|_k = p^2 + \frac{3\lambda_\phi}{2} [2k^2 \tilde{I}_{\text{pol}}(\sqrt{2}k, \sqrt{2}k, p^2)]_k^\Lambda. \tag{E7}$$

Performing the Wick rotation of (E7) and extracting the spectral function with 2, we find that the one-loop scattering contribution to the spectral function is discontinuous at $\omega = 2\sqrt{2\Lambda^2} = 2m_{\text{pole}}^\Lambda$ and turns negative for larger spectral values. Clearly, leading-order information is lost above the initial onset scale and cannot be recovered by the flow. Even worse, for higher frequencies than $2m_{\text{pole}}^\Lambda$, the positivity of the spectral function is violated. This is cured by using RG-consistent initial conditions, which appears to be crucial to obtain a physical spectral function from the flow. To that end, we require the solution to be independent of the initial scale Λ. This can be achieved by sending the initial scale to infinity, corresponding to an initial condition that cancels the Λ dependence trivially. This is done by choosing the initial condition to be an iterative solution of

$$\begin{aligned}&\Gamma^{(2)}[p^2, Z_\phi, \Gamma^{(3)}, m_{\text{pole}}] \\ &= m_{\text{pole}}^2 + p^2 - \frac{1}{2}\frac{(\Gamma^{(3)})^2}{Z_\phi^3} \\ &\quad \times [\tilde{I}_{\text{pol}}(m_{\text{pole}}, m_{\text{pole}}, p^2) - \tilde{I}_{\text{pol}}(m_{\text{pole}}, m_{\text{pole}}, -m_{\text{pole}}^2)],\end{aligned} \tag{E8}$$

where the last term accounts for the on-shell renormalization. As an initial guess, we use the parameter of the classical effective potential [Eqs. (39) and (40)] with $Z_\phi = 1$ and $m_{\text{pole}}^2 = 2\Lambda^2$. In other words, we choose our initial condition to be compatible with (E2). Note that with this choice of initial conditions, the loss of leading-order information is circumvented at all momentum scales, as all contributions of order $O(\lambda/k)$ are taken into account. The flow is initialized at large cutoff scales, where higher terms in $\lambda_{\text{eff}} = \lambda_\phi/k$ are strongly suppressed. To determine the three-point function dynamically, Eq. (E8) was coupled to the resummed four-point function via (39). The initial values for Z_ϕ and $\Gamma^{(3)}$ are presented in Table II.

It remains for us to determine the flow of the vertices and η. These have exact diagrammatic expressions, which are in parts necessary to consider. It is convenient to approximate $\partial_t \Gamma^{(4)}$ by the t-derivative of (27), where we only consider the contributions of the mass pole for simplicity. It leads to

TABLE II. Initial conditions obtained from (E8). We measure the initial RG scale Λ in units of the coupling and every other quantity in units of the mass.

Λ/λ_ϕ	$\Gamma^{(3)}[\lambda_\phi^{\frac{3}{2}}]$	Z_ϕ
10	17.3084	1.0007

$$\begin{aligned}\partial_t \Gamma^{(4)} &\approx \frac{(1-2\eta_\phi)}{Z_\phi^2} \frac{(\Gamma^{(4)})^2}{16\pi\sqrt{2}k}, \\ (\partial_t)^2 \Gamma^{(4)} &\approx \frac{2(\partial_t \Gamma^{(4)})^2}{\Gamma^{(4)}} - \partial_t \Gamma^{(4)} \\ &\quad + \frac{(\eta_\phi(1-2\eta_\phi) - \dot{\eta}_\phi)}{Z_\phi^2} \frac{(\Gamma^{(4)})^2}{8\pi\sqrt{2}k}.\end{aligned} \tag{E9}$$

The explicit k dependences of (E9) can now be taken into account analytically in (E2). For η_ϕ, we use the definition of Z_ϕ as the residue on the mass pole:

$$Z_\phi = -\partial_{\omega^2} \Gamma^2(\omega^2)|_{\omega^2 = m_{\text{pole}}^2}. \tag{E10a}$$

With the parametrization of the real part of the inverse propagator as

$$\Gamma^{(2)}(\omega^2) = Z(\omega)(m_{\text{pole}}^2 - \omega^2), \tag{E10b}$$

the anomalous dimension η_ϕ is computed conveniently from the momentum derivative of the flow on the mass pole,

$$\eta_\phi = \frac{1}{Z_\phi} \partial_{\omega^2} \frac{d}{dt} \Gamma^2(\omega^2)|_{m_{\text{pole}}^2} - \frac{1}{Z_\phi} 4k^2 \partial_{\omega^2} Z(\omega)|_{m_{\text{pole}}^2}. \tag{E10c}$$

Only the diagrams of (B6) contribute due to the momentum derivative. The second term is given in terms of the spectral function:

$$\partial_{\omega^2} Z(\omega)|_{\omega^2 = m_{\text{pole}}^2} = \frac{1}{Z_\phi} \int_\lambda \frac{\rho(\lambda)}{\lambda^2 - m_{\text{pole}}^2}. \tag{E11}$$

The other parameters, such as $\dot{\eta}_\phi$ and $\partial_t \Delta m_{\text{curv}}^2$, were approximated by a numerical right derivative.

2. Numerical implementation

The numerical implementation uses *Mathematica* [44]. The leading-order contribution to the flow was integrated by means of (E2), where we split the explicit k dependencies of each term from the subleading running of the respective parameter. This was facilitated by the split of the tree-level curvature mass: $m_{\text{curv}}^2 = Z_\phi(2k^2) + \Delta m_{\text{curv}}^2$, as it allowed us to incorporate the tree-level running of the integrand in (E2) analytically. The subleading corrections

to the flow parameter were approximated as constants in each step, while the combined k dependence of $\tilde{I}_{\mathrm{pol}}$ and the tree-level k dependence of m^2_{curv} and $\partial_t\Gamma^{(4)}$ was integrated analytically.

For the one-cut contributions, including the tadpole, we approximated the k-integral by an explicit Euler scheme. For the sake of computation time, higher-dimensional spectral integrals were dropped, as they were numerically negligible in the considered coupling range in comparison to the leading-order and next-to-leading-order contributions. For an investigation of the scaling limit, their incorporation is crucial. The numerical integrations of spectral integrals were carried out using a global adaptive integration strategy. All contributions to diagrams were calculated and interpolated separately, where we used finer grids around sharp structures and more coarse grids where the functions are smooth. We implemented a local feedback of the spectral function with a step size $dk = 0.005$, using the spectral function ρ to calculate $\partial_t\Gamma^{(2)}$. The correct renormalization was enforced conveniently in every step by subtracting the value of the inverse propagator on the mass pole. The residue on the pole was extracted from $\Gamma^{(2)}(p)$ in each step via Eq. (E10a).

APPENDIX F: CALCULATION OF DIAGRAMS

In this section, all diagrammatic expressions appearing in the main text are given in analytic form. The spectral approach we use, allows us to calculate diagrams with full propagators in terms of integrals known from perturbation theory. The insertion of a mass-derivative in Fig. 5 leads to a squared propagator on one line in comparison with the usual vacuum polarization or tadpole diagram. Using the spectral representation, the momentum structure of the regulator line can be rewritten via a partial fraction decomposition

$$\frac{1}{(\lambda_1^2+q^2)(\lambda_2^2+q^2)} = \frac{-1}{(\lambda_1^2-\lambda_2^2)}\left(\frac{1}{\lambda_1^2+q^2}-\frac{1}{\lambda_2^2+q^2}\right). \tag{F1}$$

A given (spectral) flow diagram can therefore be reduced to the computation of the momentum integral, where the regulator line is replaced by a single propagator, which we will denote with a tilde. Denoting the spectral parameters of the divided line as λ_1 and λ_2, we write schematically

$$\mathrm{D}(\lambda_1,\lambda_2,\ldots,p^2) = \frac{-1}{(\lambda_1^2-\lambda_2^2)}[\tilde{D}(\lambda_1\ldots,p^2)-\tilde{D}(\lambda_2\ldots,p^2)], \tag{F2}$$

and accordingly

$$\mathrm{D}(\lambda,\lambda,\ldots,p^2) = \frac{-1}{2\lambda}\partial_\lambda\tilde{D}(\lambda\ldots,p^2). \tag{F3}$$

This reduces the calculation of I_{pol}, as defined in Eq. (A3b) to the calculation of $\tilde{I}_{\mathrm{pol}}$ as given below:

$$I_{\mathrm{pol}}(\lambda_1,\lambda_2,\lambda_3,p^2) = \frac{-1}{(\lambda_1^2-\lambda_2^2)}[\tilde{I}_{\mathrm{pol}}(\lambda_1,\lambda_3,p^2)-\tilde{I}_{\mathrm{pol}}(\lambda_2,\lambda_3,p^2)]. \tag{F4}$$

Denoting the Euclidean and Minkowskian frequencies by p and ω, respectively, the momentum structure of the spectral polarization diagram reads

$$\begin{aligned}\tilde{I}_{\mathrm{pol}}(p,\lambda_1,\lambda_2) &= \frac{1}{4\pi p}\,\mathrm{Arctan}\left[\frac{p}{\lambda_1+\lambda_2}\right],\\ \tilde{I}_{\mathrm{pol}}(\omega,\lambda_1,\lambda_2) &= \frac{1}{4\pi\omega}\left\{\mathrm{Arctanh}\left[\frac{w}{\lambda_1+\lambda_2}\right]\right.\\ &\quad\left.+\,\mathrm{i}\theta(\omega-(\lambda_1+\lambda_2))\right\};\end{aligned} \tag{F5}$$

see [1,45]. We find the integrand I_{pol} of the polarization diagram to have a branch cut with compact support, i.e., for $\omega\in[\lambda_1+\lambda_3,\lambda_2+\lambda_3]$ for $\lambda_1\le\lambda_2$. This peculiarity is a dimension-dependent property of the polarization diagram which does not hold in four dimensions. There, the imaginary part of I_{pol} has support for $\omega\in[\lambda_1+\lambda_3,\infty)$ for $\lambda_1\le\lambda_2$.

The onset position of these structures allows us to discuss the scattering continua. To this end, we note that the diagrams with a polarization topology have two or three lines that can carry either a mass pole or a scattering contribution; see Fig. 7. If all lines carry a pole contribution, which is the leading order for all couplings in the considered coupling range, we find the flow of a discontinuity seeded at $2m_{\mathrm{pole}}$, representing a $1\to2$ scattering.

APPENDIX G: HIGHER-ORDER CONTRIBUTIONS TO $\mathrm{Im}\Gamma^{(2)}$

In this section, we discuss the feedback of the scattering continuum and present the next-to-leading-order contributions. We restrict ourselves to the imaginary part, since it carries the dominant features. In contrast, the contributions of the respective real parts to the spectral function cannot be separated from each other, as they only appear in the denominator of Eq. (2b). Inserting exactly one scattering continuum in one of the top lines of the polarization diagram, we find a contribution adding to both the $1\to2$ and the $1\to3$ onset, consequently also starting at $2m_{\mathrm{pole}}$, as can be seen in the top panel of Fig. 13. The dominant sharp onsets of the $1\to3$ scattering are found in the polarization diagram by inserting exactly one scattering continuum into the bottom line and into the tadpole. Their integrated flows are presented in the middle and lower panels of Fig. 13. Note that they correspond to different diagrammatic topologies. The $1\to3$ contribution of the polarization diagram can be described diagrammatically by two consecutive

$1 \to 2$ scatterings, whereas the tadpole reproduces a sunset topology. The insertion of two or three scattering continua lead to sharp—although strongly suppressed—onsets at $3m_{\rm pole}$ and $4m_{\rm pole}$.

In Fig. 13, the one-cut corrections to the imaginary part are given in units of their respective coupling strength. The rescaled contributions are qualitatively compatible with each other, showing the proportionality of the one-cut contribution to λ_ϕ^2. This can be anticipated from two-loop perturbation theory. The decrease of the peak for higher couplings is connected to the decrease of the residue Z^{-1} of the mass pole, as shown in Fig. 10(a). The tadpole contribution is at leading order proportional to λ_ϕ^2. On a perturbative level, the first dynamic contribution is introduced by the first bubble diagram in Fig. 8. This is confirmed in the third panel of Fig. 13, where the different tadpole contributions share the same order of magnitude if rescaled with λ_ϕ^2.

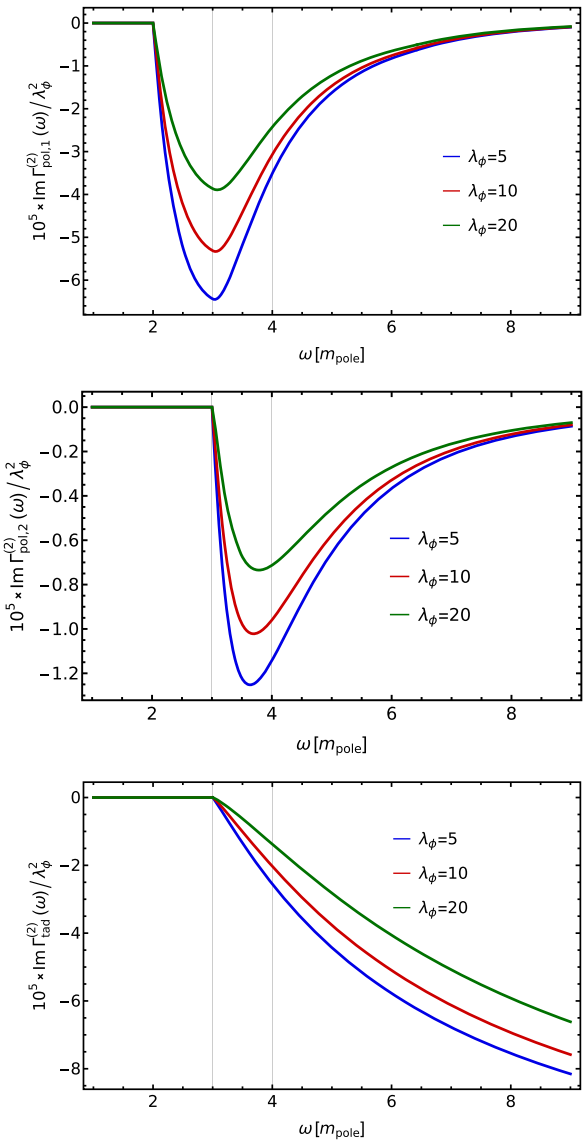

FIG. 13. Next-to-leading-order contributions to the imaginary part of the integrated flow in the broken phase rescaled by λ_ϕ^2. All dimensionful quantities are measured in units of the pole mass. The first two figures show the contributions of the polarization diagram. They start at $2m_{\rm pole}$ and $3m_{\rm pole}$, respectively. The third figure is the dominating tadpole contribution, i.e., the insertion of ρ_4 for the vertex and only the *pole* contributions for the propagators. It exhibits only a three-particle onset, as discussed in Sec. V A.

APPENDIX H: FLOW EQUATION OF THE EFFECTIVE POTENTIAL

In this section, we briefly discuss the flow equation of the effective potential in the local potential approximation for the sake of completeness and for the illustration of consistency of the approach. Its derivation, including the determination of the counterterm, has been discussed in detail in Appendix A of Ref. [8]. The flow of the first field derivative of the effective potential in three dimensions is given by

$$\partial_\mu V^{(1)}_{\rm eff}(\phi) = -\frac{1}{2}\int \frac{\mathrm{d}^3 p}{(2\pi)^3} \frac{V^{(3)}_{\rm eff}(\phi)}{[p^2 + V^{(2)}_{\rm eff}(\phi)]^2} + \phi - \partial_\mu S^{(1)}_{\rm ct}[\phi], \tag{H1}$$

where we have dropped the multiplication with μ present in Eq. (14). We have already used the fact that the momentum integral in (H1) is finite, and hence we can remove additional regularizations such as dimensional regularization relevant in the $d = 4$ case; see again Appendix A of [8]. The momentum integral in (H1) is readily performed, and we arrive at

$$\partial_\mu V^{(1)}_{\rm eff}(\phi) = -\frac{1}{4\pi^2} \frac{V^{(3)}_{\rm eff}(\phi)}{\sqrt{V^{(2)}_{\rm eff}(\phi)}} + \phi - \partial_\mu S^{(1)}_{\rm ct}[\phi], \tag{H2}$$

and upon ϕ-integration, we are led to

$$\partial_\mu V_{\rm eff}(\phi) = -\frac{1}{8\pi^2}\sqrt{V^{(2)}_{\rm eff}(\phi)} + \frac{1}{2}\phi^2 - \partial_\mu S_{\rm ct}[\phi], \tag{H3}$$

where we have set the integration constant to zero. Note that (H3) has a peculiar form: the loop contribution is negative, while its diagrammatic form is seemingly positive, but not well defined without regularization. We emphasize that the first field derivative of the flow in (H3) is negative (times $V^{(3)}_{\rm eff}$) [see (H2)], as holds true for all momentum-cutoff flows.

It is illustrative to consider the large field limit with $\phi^2/|\mu| \to \infty$. For these field values, the effective potential (or rather its interaction part) reduces to the classical one, and the flow reduces to

$$\partial_\mu V_{\text{eff}}(\phi) \to -\frac{1}{8\pi^2}\sqrt{\frac{\lambda_\phi}{2}\phi^2} + \frac{1}{2}\phi^2 - \partial_\mu S_{\text{ct}}[\phi], \quad \text{(H4)}$$

up to subleading terms. We note in passing that (H4) shows the self-consistency of the assumption that the interaction part reduces to the classical one. The right-hand side is proportional to $|\phi| = \sqrt{2\rho}$. This reflects the infrared cut in three-dimensional momentum cutoff flows for $\mu \to 0$. For the CS flow, it is present for all μ in the large field limit, in contradistinction to momentum cutoff flows that decay with $1/V^{(2)}_{\text{eff}}(\phi)$ for large fields.

[1] J. Horak, J. M. Pawlowski, and N. Wink, Spectral functions in the ϕ^4-theory from the spectral DSE, Phys. Rev. D **102**, 125016 (2020).

[2] J. Horak, J. Papavassiliou, J. M. Pawlowski, and N. Wink, Ghost spectral function from the spectral Dyson-Schwinger equation, Phys. Rev. D **104**, 074017 (2021).

[3] J. Horak, J. M. Pawlowski, and N. Wink, On the complex structure of Yang-Mills theory, arXiv:2202.09333.

[4] J. Horak, J. M. Pawlowski, and N. Wink, On the quark spectral function in QCD, SciPost Phys. **15**, 149 (2023).

[5] G. Eichmann, A. Gómez, J. Horak, J. M. Pawlowski, J. Wessely, and N. Wink, Bound states from the spectral Bethe-Salpeter equation, Phys. Rev. D **109**, 096024 (2024).

[6] G. Kallen, On the definition of the renormalization constants in quantum electrodynamics, Helv. Phys. Acta **25**, 417 (1952).

[7] H. Lehmann, On the properties of propagation functions and renormalization contants of quantized fields, Nuovo Cimento **11**, 342 (1954).

[8] J. Braun *et al.*, Renormalised spectral flows, SciPost Phys. Core **6**, 061 (2023).

[9] J. Fehre, D. F. Litim, J. M. Pawlowski, and M. Reichert, Lorentzian quantum gravity and the graviton spectral function, Phys. Rev. Lett. **130**, 081501 (2023).

[10] J. Alexandre and J. Polonyi, Functional Callan-Symanzik equation, Ann. Phys. (N.Y.) **288**, 37 (2001).

[11] S. Correia, J. Polonyi, and J. Richert, Functional Callan-Symanzik equation for the Coulomb gas, Ann. Phys. (Amsterdam) **296**, 214 (2002).

[12] J. Alexandre, J. Polonyi, and K. Sailer, Functional Callan-Symanzik equation for QED, Phys. Lett. B **531**, 316 (2002).

[13] T. Gasenzer and J. M. Pawlowski, Towards far-from-equilibrium quantum field dynamics: A functional renormalisation-group approach, Phys. Lett. B **670**, 135 (2008).

[14] T. Gasenzer, S. Kessler, and J. M. Pawlowski, Far-from-equilibrium quantum many-body dynamics, Eur. Phys. J. C **70**, 423 (2010).

[15] S. Floerchinger, Analytic continuation of functional renormalization group equations, J. High Energy Phys. 05 (2012) 021.

[16] K. Kamikado, N. Strodthoff, L. von Smekal, and J. Wambach, Real-time correlation functions in the O(N) model from the functional renormalization group, Eur. Phys. J. C **74**, 2806 (2014).

[17] R.-A. Tripolt, N. Strodthoff, L. von Smekal, and J. Wambach, Spectral functions for the quark-meson model phase diagram from the functional renormalization group, Phys. Rev. D **89**, 034010 (2014).

[18] J. M. Pawlowski and N. Strodthoff, Real time correlation functions and the functional renormalization group, Phys. Rev. D **92**, 094009 (2015).

[19] K. Kamikado, T. Kanazawa, and S. Uchino, Mobile impurity in a Fermi sea from the functional renormalization group analytically continued to real time, Phys. Rev. A **95**, 013612 (2017).

[20] C. Jung, F. Rennecke, R.-A. Tripolt, L. von Smekal, and J. Wambach, In-medium spectral functions of vector- and axial-vector mesons from the functional renormalization group, Phys. Rev. D **95**, 036020 (2017).

[21] J. M. Pawlowski, N. Strodthoff, and N. Wink, Finite temperature spectral functions in the $O(N)$-model, Phys. Rev. D **98**, 074008 (2018).

[22] Z. Wang and P. Zhuang, Meson spectral functions at finite temperature and isospin density with the functional renormalization group, Phys. Rev. D **96**, 014006 (2017).

[23] R.-A. Tripolt, C. Jung, N. Tanji, L. von Smekal, and J. Wambach, In-medium spectral functions and dilepton rates with the functional renormalization group, Nucl. Phys. **A982**, 775 (2019).

[24] R.-A. Tripolt, J. Weyrich, L. von Smekal, and J. Wambach, Fermionic spectral functions with the functional renormalization group, Phys. Rev. D **98**, 094002 (2018).

[25] L. Corell, A. K. Cyrol, M. Heller, and J. M. Pawlowski, Flowing with the temporal renormalization group, Phys. Rev. D **104**, 025005 (2021).

[26] S. Huelsmann, S. Schlichting, and P. Scior, Spectral functions from the real-time functional renormalization group, Phys. Rev. D **102**, 096004 (2020).

[27] C. Jung, J.-H. Otto, R.-A. Tripolt, and L. von Smekal, Self-consistent $O(4)$ model spectral functions from analytically continued functional renormalization group flows, Phys. Rev. D **104**, 094011 (2021).

[28] Y.-y. Tan, Y.-r. Chen, and W.-j. Fu, Real-time dynamics of the $O(4)$ scalar theory within the fRG approach, SciPost Phys. **12**, 026 (2022).

[29] M. Heller and J. M. Pawlowski, Causal temporal renormalisation group flow of the energy-momentum tensor, arXiv:2112.12652.

[30] J. V. Roth, D. Schweitzer, L. J. Sieke, and L. von Smekal, Real-time methods for spectral functions, Phys. Rev. D **105**, 116017 (2022).

[31] J. V. Roth and L. von Smekal, Critical dynamics in a real-time formulation of the functional renormalization group, J. High Energy Phys. 10 (2023) 065.

[32] J. Horak, J. M. Pawlowski, J. Rodríguez-Quintero, J. Turnwald, J. M. Urban, N. Wink, and S. Zafeiropoulos, Reconstructing QCD spectral functions with Gaussian processes, Phys. Rev. D **105**, 036014 (2022).
[33] J. Horak, J. M. Pawlowski, J. Turnwald, J. M. Urban, N. Wink, and S. Zafeiropoulos, Non-perturbative strong coupling at timelike momenta, Phys. Rev. D **107**, 076019 (2023).
[34] K. Symanzik, Small distance behavior in field theory and power counting, Commun. Math. Phys. **18**, 227 (1970).
[35] C. Wetterich, Exact evolution equation for the effective potential, Phys. Lett. B **301**, 90 (1993).
[36] N. Dupuis, L. Canet, A. Eichhorn, W. Metzner, J. M. Pawlowski, M. Tissier, and N. Wschebor, The nonperturbative functional renormalization group and its applications, Phys. Rep. **910**, 1 (2021).
[37] M. Caselle, M. Hasenbusch, P. Provero, and K. Zarembo, Bound states and glueballs in three-dimensional Ising systems, Nucl. Phys. **B623**, 474 (2002).
[38] V. Agostini, G. Carlino, M. Caselle, and M. Hasenbusch, The spectrum of the $(2+1)$-dimensional gauge Ising model, Nucl. Phys. **B484**, 331 (1997).
[39] M. Caselle, M. Hasenbusch, and P. Provero, Nonperturbative states in the 3D ϕ^4 theory, Nucl. Phys. **B556**, 575 (1999).
[40] F. Rose, F. Benitez, F. Léonard, and B. Delamotte, Bound states of the ϕ^4 model via the nonperturbative renormalization group, Phys. Rev. D **93**, 125018 (2016).
[41] K. Kockler, J. M. Pawlowski, and J. Wessely, Scaling spectral functions from the spectral fRG (to be published).
[42] J. Braun *et al.*, fQCD Collaboration (2023).
[43] A. Bonanno, T. Denz, J. M. Pawlowski, and M. Reichert, Reconstructing the graviton, SciPost Phys. **12**, 001 (2022).
[44] W. R. Inc., *Mathematica*, Version 13.1, Champaign, IL, 2022, https://www.wolfram.com/mathematica.
[45] A. K. Rajantie, Feynman diagrams to three loops in three-dimensional field theory, Nucl. Phys. **B513**, 761 (1998); **B480**, 729(E) (1996).